



The Modeling of Time-Dependent Deformation and Fracturing of Brittle Rocks Under Varying Confining and Pore Pressures

Tao Xu^{1,2} · Guanglei Zhou^{1,2} · Michael J. Heap³ · Shengqi Yang⁴ · Heinz Konietzky⁵ · Patrick Baud³

Received: 29 September 2017 / Accepted: 23 April 2018
© Springer-Verlag GmbH Austria, part of Springer Nature 2018

Abstract

A numerical hydro-mechanical model for brittle creep is proposed to describe the time-dependent deformation of heterogeneous brittle rock under constant confining and pore pressures. Material heterogeneity and a local material degradation law are incorporated into the model at the mesoscale which affects the mechanical behavior of rocks to capture the co-operative interaction between microcracks in the transition from distributed to localized damage. The model also describes the spatiotemporal acoustic emissions in the rock during the progressive damage process. The approach presented in this contribution differs from macroscopic approaches based on constitutive laws and microscopic approaches focused on fracture propagation. The model is first validated using experimental data for porous sandstone and is then used to simulate brittle creep tests under varying constant confining and pore pressures and applied differential stresses. We further explore the influence of sample homogeneity on brittle creep. The model accurately replicates the classic creep behavior observed in laboratory brittle creep experiments. In agreement with experimental observations, our model shows that decreasing effective pressure, increasing the applied differential stress, and decreasing sample homogeneity increase the creep strain rate and decrease the time-to-failure, respectively. The model shows that complex macroscopic time-dependent behavior can be explained by the microscale interaction of elements. The fact that the simulations are able to capture a similar hydro-mechanical time-dependent response to that of laboratory experiments implies that the model is an appropriate tool to investigate the complex time-dependent behavior of heterogeneous brittle rocks under coupled hydro-mechanical loading.

Keywords Time-dependent deformation · Pore pressure · Differential stress · Creep strain rate · Numerical simulation

✉ Tao Xu
xutao@mail.neu.edu.cn; neuxutao@126.com

¹ Key Laboratory of Ministry of Education on Safe Mining of Deep Metal Mines, Northeastern University, Shenyang 110819, People's Republic of China

² Center for Rock Instability and Seismicity Research, Northeastern University, Shenyang 110819, People's Republic of China

³ Géophysique Expérimentale, Institut de Physique de Globe de Strasbourg (UMR 7516 CNRS, Université de Strasbourg/EOST), 5 rue René Descartes, 67084 Strasbourg Cedex, France

⁴ State Key Laboratory for Geomechanics and Deep Underground Engineering, School of Mechanics and Civil Engineering, China University of Mining and Technology, Xuzhou 221116, People's Republic of China

⁵ Geotechnical Institute, TU Bergakademie Freiberg, Gustav-Zeuner-Str. 1, 09596 Freiberg, Germany

List of Symbols

A	Material constant
D	Damage variable
e_f	Energy released from a failed element
e_{ij}	Strain deviator of the elastic strain components
E, E_0	Young's moduli of damaged material and undamaged material
f_i	Body forces per unit volume
F_1, F_2	Tensile and shear damage threshold functions
f_{t0}, f_{c0}	Uniaxial tensile strength and uniaxial compressive strength
G	Shear modulus
h	The convective heat transfer coefficient
k	The coefficient of permeability
K', K_s	Bulk modulus of the porous medium, and effective bulk modulus of the solid constituent
m	A fraction constant
n	Stress component of greater than one
n_i	The number of failed elements in the i th step
N	Total number of elements

P, P_{eff}	Fluid pore pressure and effective pressure
R	Universal gas constant
r	Constitutive coefficient
S_{ij}	Stress deviator tensor of the elastic stress components
T	Absolute temperature
U	Creep activation energy
ν_e	The volume of single element
V_f, V	The volume of failed elements, the total volume of all elements
α	Biot's efficient
φ	Porosity
β_1	The bulk modulus of fluid
ε	Total strain
$\varepsilon_1, \varepsilon_3$	The maximum and minimum principal strain
ε_C	Creep strain
ε_e	Elastic strain
ε_{ij}	Small strain tensor
$\varepsilon_{t0}, \varepsilon_{c0}$	The maximum tensile and compressive strain
$\varepsilon_{tr}, \varepsilon_{cr}$	The residual tensile and compressive strain corresponding to residual strength
ε_{tu}	The ultimate tensile strain corresponding to complete damage
K	The intrinsic permeability in a general continuum
ρ_l	The fluid density
u, u_0	Scale parameter of an element, the average element parameter
u_i	Mechanical parameter of the element i
μ_l	The dynamic fluid viscosity
δ_{ij}	Kronecker delta
λ	Lame's constant
ζ	Residual strength coefficient
η	Ultimate tensile strain coefficient
ρ	Bulk density of medium
χ	Homogeneity index
ϕ	Angle of internal friction
ω_i	Random numbers ranging from 0 to 1
ψ	The ratio of the volume of failed rock to total volume of rock
ξ	The factor that reflects damage-induced permeability increase
σ_e	Effective stress
σ_{ij}	Total stress tensor
σ_{ii}	Average stress
σ_1, σ_2	The maximum and minimum principal stress

1 Introduction

The stressed rock mass in most rock engineering structures (deep underground rock engineering, high-slope rock engineering, dam engineering, and radioactive waste disposal) is either saturated with water or subjected to high humidity

levels. The presence of the water in rock not only affects the mechanical behavior of rocks (e.g., Baud et al. 2000; Duda and Renner 2012), but also allows chemical interactions between water and rock to occur (e.g., Brantut et al. 2013). The mechanical effect, which results in rock failure at lower applied differential stresses, is caused by an increase in pore or joint water pressure that reduces the effective stress and the applied normal stress acting on the rock mass. The chemical effects are more difficult to interpret as they involve complex chemical reactions between the rock and the water or water vapor. The chemical effects usually weaken the rock via the reduction of surface free energy due to the absorption of pore water into the internal pore surfaces (Andrade and Randall 1949; Baud et al. 2000) and by promoting subcritical crack growth due to stress corrosion (Atkinson and Meredith 1981; Meredith and Atkinson 1983; Brantut et al. 2013). In the design of complex rock engineering projects, neglecting the influence of time-dependent deformation could provide models that do not accurately capture the trends seen in field measurements (Maranini and Brignoli 1999; Weng et al. 2010), which may lead to an incorrect evaluation or even a serious disaster. Moreover, elevated pore pressures (i.e., reduced effective pressures) likely impart a significant influence on the time-dependent behavior of the host rock, and consequently affect the overall long-term performance of rock engineering projects. Therefore, a good understanding through the reliable modeling of the time-dependent behavior of the host rock under elevated pore pressure (i.e., reduced effective pressure) is essential for stability and safety assessments in rock engineering (Peng et al. 2010).

The influence of confining and pore pressure on the time-dependent deformation of rock is of great importance in the upper crust (Brantut et al. 2013). Indeed, many studies have investigated the time-dependent behavior of soft rocks such as sedimentary rocks (Carter and Hansen 1983; Cristescu 1993; Baud and Meredith 1997; Dubey and Gairola 2008; Heap et al. 2009a, b, 2015; Okubo et al. 2010; Yang et al. 2014; Brantut et al. 2014a, b; Nicolas et al. 2017) and hard rocks such as granite or basalt (Kranz 1980; Lajtai et al. 1987; Lockner 1993a, b; Katz and Reches 2002; Lin et al. 2009; Heap et al. 2011). Baud et al. (2000) investigated water weakening in porous sandstones and found that the presence of water reduced the strength of sandstones. Wasantha et al. (2014) investigated the mechanical behavior and the energy-releasing characteristics of dry and saturated bedded sandstone by adopting the acoustic emission (AE) technique. Heap et al. (2009a) reported the results from a study of time-dependent brittle creep in water-saturated samples of Darley Dale sandstone under triaxial stress conditions and found that, for a given differential stress, creep strain rates are considerably lower at high effective pressures. Yang et al. (2014) performed an experimental study on short-term

and creep tests on saturated red sandstone under different effective pressures. Xu and Yang (2016) analyzed the permeability of sandstone under increasing differential stress in both short-term and brittle creep experiments. Brantut et al. (2013) reviewed our understanding of time-dependent cracking and brittle creep in crustal rocks and pointed out that an extension of the range of available laboratory data to lower strain rates and the development of new modeling approaches are needed to further improve our current understanding of time-dependent brittle deformation in rocks. However, the above-mentioned investigations mainly focus on the study of brittle creep in the laboratory and few numerical studies have been performed on coupled hydro-mechanical creep in brittle rocks.

During a brittle creep experiment, in which a rock sample is held at a constant differential stress for an extended period of time, the strain against time (the “creep curve”) first decelerates before accelerating as macroscopic sample failure is approached (Brantut et al. 2013). The onset of the acceleration to failure in brittle creep experiments has been ascribed as the result of the sample reaching a microcrack density at which microcracks can interact and coalesce, sometimes referred to as the “critical damage threshold” (Kranz and Scholz 1977; Baud and Meredith 1997; Heap et al. 2009a, 2011; Xu et al. 2012). The acceleration in strain rate during this accelerating phase has been previously described using a power law (Voight 1989; Bell et al. 2011a, b).

Time-dependent brittle deformation is often attributed to a mechanism of subcritical crack growth called stress corrosion cracking (Atkinson 1984; Brantut et al. 2013). Stress corrosion describes fluid-rock reactions that occur preferentially between a chemically active pore fluid and strained atomic bonds at the crack tips and is therefore sensitive to environmental factors such as stress, temperature, and pore fluid reactivity (Atkinson 1984). An important aspect is the influence of the presence of a pore fluid, which significantly decreases the specific fracture energy and hence the fracture toughness of sandstones (Baud et al. 2000). Indeed, experiments on Westerly granite (Kranz et al. 1982) have shown that times-to-failure are shorter by around three orders of magnitude under saturated conditions than under ambient humidity conditions.

Based on experimental investigations, various creep models have been proposed over the last few decades, which can be grouped into three classes: empirical models, component models, and mechanism-based constitutive models. Empirical models, based on laboratory investigations, are widely used in engineering (Cristescu 1993). However, due to the difference in timescale between laboratory investigations and the timescale of interest in engineering projects, the validation and suitability of these models in the long-term prediction are dubious. Component models (Maranini

and Yamaguchi 2001), which are generally a combination of standard elements such as the Newtonian dashpot, the Hooke spring, and the frictional element, have the advantage of a flexible description of the different creep deformations. The use of viscoplastic models such as Perzyna viscoplastic model for describing the non-linear and rate-sensitive behavior of other geomaterials, such as clays, is well established and many rheological models have been issued from this formalism (Perzyna 1966, 1971; Pan and Wan-xie 1991; Wang et al. 2015). The Perzyna viscoplastic model is implemented by allowing the stress state to be outside the yield surface and directly define the plastic relaxation equations in the stress space. However, the formulation of these models is always complex and often lacks physical meaning. In recent years, a mechanism-based creep model has been developed based on cracking and damage evolution at the microscale (Lockner and Madden 1991; Yoshida and Horii 1992; Shao et al. 1997; Amitrano and Helmstetter 2006; Chen and Konietzky 2014; Li and Konietzky 2014; Lu et al. 2014; Li et al. 2016; Xu et al. 2017); this type of model tries to build a bridge between phenomenology and micromechanisms (Shao et al. 2003, 2006). Micromechanical models have also successfully captured brittle creep behavior in rock (Brantut et al. 2012) and glass (Mallet et al. 2015).

Due to the aforementioned importance of understanding the long-term mechanical behavior of rock in deep underground rock engineering projects, high slope rock engineering projects, dam engineering projects, and radioactive waste disposal, we present here a hydro-mechanical constitutive model to describe the time-dependent deformation of brittle rocks under different constant pore and confining pressures. We also model the accompanying AEs, which are considered as a macroscopic consequence of the progressive degradation of the material at the mesoscale. First, we formulate the hydro-mechanical coupled time-dependent model and validate the model with experimental data. We then present and discuss the results of the brittle creep simulations and compare them with the wealth of available experimental data and observations.

2 Formulation of Time-Dependent Constitutive Model

In this section, we propose a quantitative model for the coupled water flow and time-dependent deformation of a stressed rock, and we further develop the numerical code for hydro-mechanical time-dependent deformation of rock to investigate time-dependent deformation of rock at different pore and confining pressures. When formulating the model in mathematical language, various levels of complexity should be incorporated into each component, with the accuracy and versatility of the model depending

on the refinement of the description of each component. For a model used to investigate hydro-mechanical time-dependent deformation of a stressed rock, the coupled effect between the deformed medium and water flow is very important. Three components should be considered: a fluid flow description, a creep and stress description, and a description of the evolution of damage. The descriptions of these components will now be discussed in turn.

The model is based on the theory of elastic damage mechanics and assumes that the damage is elastic and isotropic. The model accounts for material heterogeneity through a stochastic local failure stress field, and then uses solid mechanics and fluid flow to calculate the stress distribution. Every step local material degradation is calculated using an exponential material softening law (i.e., different to the approach adopted by Amitrano and Helmstetter 2006). The maximum tensile strain criterion and a modified Mohr–Coulomb criterion with a tension cut-off are adopted as two failure thresholds in the model. The tensile strain criterion is always used with priority to judge whether the element is damaged (since, as discussed above, rock is weaker in tension than in compression). If the element is not damaged in tension, the Mohr–Coulomb criterion is then used to judge whether the element is damaged in shear. According to the constitutive law, the damage variable calculated is always from zero to one regardless of the type of damage (tensile or shear). If any of the elements in a stressed specimen are damaged, the damaged elements will undergo a degradation of their elastic modulus ($E = E_0(1 - D)$) according to the elastic damage constitutive relationship. In this model, $D = 1$ corresponds to the complete failure of the element, and the elastic modulus of this element tends to zero. If the damage variable D of the element less than 1, then the element will be still calculated in the next step until the whole model is failed or this element is completely failed. This approach makes it possible to simulate the transition from distributed damage by tensile microcracking to damage where microcracks can interact, coalesce, and ultimately form a shear fault. The model also describes the temporal and spatial evolution of AEs, including their size (energy released), in the medium during the progressive damage process. Furthermore, the model can visually replicate the tempo-spatial evolution of the shear stress fields and a rich assortment of other parameters, such as compressive stress, tensile stress, displacement vector, and flow vector during the time-dependent brittle deformation of heterogeneous rock under a constant compressive stress and pore and confining pressures.

2.1 Fluid Flow Description

The fundamental assumption behind the model presented here is that the rock is elastic and saturated with a fluid such

as water. As a result, the equation for fluid flow in porous media should be used. The equation that governs the fluid flow in a porous medium is known as Darcy's law

$$q_1 = -k\nabla(P + \rho_1gz), \quad (1)$$

where P is pore fluid pressure, z is the vertical coordinate, k is the coefficient of permeability [$\text{m}^4/(\text{N s})$] with $k = \kappa/\mu_1$, where μ_1 is the dynamic fluid viscosity (N s/m^2), κ is the intrinsic permeability in a general continuum (m^2), ρ_1 is the fluid density (kg/m^3), and g is the acceleration due to surface gravity (m/s^2). The substitution of Eq. (1) into the conservation equation of fluid results in (Biot 1956):

$$c_1 \frac{\partial \varepsilon_V}{\partial t} + c_2 \frac{\partial P}{\partial t} = \nabla[k(\nabla P + \rho_1g\nabla z)], \quad (2)$$

$$c_1 = 1 - \frac{K'}{K_S} \quad \text{and} \quad c_2 = \frac{\varphi}{\beta_1} + \frac{(1 - \varphi)}{K_S}, \quad (3)$$

where φ is the porosity, β_1 denotes the bulk modulus of fluid, K_S is the effective bulk modulus of the solid constituent, and K' ($K' = 2G(1 + \mu)/3(1 - 2\mu)$) is the drained bulk modulus of the porous medium.

2.2 Creep and Stress Description

It is assumed here that the total strain for a stressed medium is the sum of three components: elastic strain, plastic strain, and creep strain. Plastic strain is not considered in our model since we focus on brittle creep. The total strain can therefore be decomposed as follows:

$$\varepsilon = \varepsilon_e + \varepsilon_c \quad (4)$$

where the subscripts e and c refer to the elastic strain and creep strain, respectively. The elastic strain ε_e can be expressed in a tensor form of Hooke's law for an elastic medium:

$$\varepsilon_e = \varepsilon_{ij} = \frac{1}{2G}S_{ij} + \frac{1}{3}\varepsilon_{kk}\delta_{ij}, \quad (5)$$

where G is the shear modulus and ε_{ij} is the strain tensor form of the elastic strain ε_e , and S_{ij} is the stress deviator tensor of the elastic stress components σ_{ij} , $S_{ij} = \sigma_{ij} - \frac{1}{3}\sigma_{kk}\delta_{ij}$, in which δ_{ij} is the Kronecker delta. The Kronecker delta equals zero when $i \neq j$ and one when $i = j$.

The creep strain ε_c is in fact a function of the stress σ , temperature T , and time t , i.e., $\varepsilon_c = F(\sigma, T, t)$. It is customary to assume that the effects are separable and are written as:

$$\varepsilon_c = f(\sigma)g(T)h(t), \quad (6)$$

where (σ) , $g(T)$ and $h(t)$ are the functions related to stress, temperature, and time, respectively.

For creep problems, a constitutive law of the creep strain rate, a Norton–bailey equation (Heard 1976; Carter and Hansen 1983), was adopted to characterize time-dependent creep deformation based on the approach of the equation of state theory:

$$\epsilon_c = A\sigma^n t^m \exp\left(-\frac{U}{RT}\right), \tag{7}$$

where A , m , and n are the constants that are a function of the temperature. The constant n usually denotes the stress component and is greater than one; m is usually a fraction; U is the creep activation energy which can be determined empirically as proportional to the slope of a plot of $\log \epsilon_c$ vs $1/T$ at constant σ , R is the universal gas constant, and T is the absolute temperature (in Kelvin).

For a time-dependent problem, the strain rate is of great interest. Hence, Eq. (7) can also be expressed in strain rate form:

$$\dot{\epsilon}_c = nA\sigma^n t^{m-1} \exp\left(-\frac{U}{RT}\right). \tag{8}$$

The creep flow rule can be expressed in tensor form under multi-axial stress conditions (Kraus 1980):

$$\dot{\epsilon}_{ij}^c = \frac{3}{2} \frac{d\bar{\epsilon}_c}{dt} \frac{S_{ij}}{\sigma_e}, \tag{9}$$

in which σ_e is the effective stress and $\sigma_e = \sqrt{\frac{3}{2} S_{ij} S_{ij}}$, $d\bar{\epsilon}_c$ is the effective creep strain, and $d\bar{\epsilon}_c = \sqrt{\frac{2}{3} d\epsilon_{ij}^c d\epsilon_{ij}^c}$. Now, if we substitute Eq. (8) into Eq. (9), the creep strain rate can be extended to the multi-axial stress case:

$$\dot{\epsilon}_{ij}^c = \frac{3}{2} An S_{ij} \sigma_e^{n-1} t^{m-1} \exp\left(-\frac{U}{RT}\right), \tag{10}$$

where $\dot{\epsilon}_{cij}$ is the creep strain rate, S_{ij} is the deviatoric part of σ_{ij} , and σ_e is the effective stress defined as

$$\sigma_e^2 = \sigma_{11}^2 + \sigma_{22}^2 + \sigma_{33}^2 - \sigma_{11}\sigma_{22} - \sigma_{22}\sigma_{33} - \sigma_{11}\sigma_{33} + 3(\sigma_{12}^2 + \sigma_{23}^2 + \sigma_{31}^2), \tag{11}$$

where σ_{11} , σ_{22} , and σ_{33} are the normal stresses and σ_{12} , σ_{23} , and σ_{31} are shear stresses. This creep model can describe decelerating creep, but it fails to accurately capture accelerating creep. Thus, a damage evolution law for accelerating creep of rock must be incorporated.

The static stress equilibrium equation for macroscopic total stresses in the absence of an inertia term can be written in the tensor form as follows:

$$\sigma_{ij,j} + f_i = 0, \tag{12}$$

where σ_{ij} is the total stress tensor ($i, j = 1, 2, 3$) in MPa and f_i is the body force per unit volume in the direction of the

coordinate axes in MPa. For a perfectly elastic isotropic continuum, the Cauchy’s infinitesimal strain tensor ϵ_{ij} is expressed in terms of the partial derivatives of the components of displacement u_i :

$$\epsilon_{ij} = \frac{1}{2} (u_{i,j} + u_{j,i}). \tag{13}$$

Thus, the constitutive stress–strain relation for an elastic isotropic medium has the following form:

$$\sigma_{ij} = \lambda \epsilon_{kk} \delta_{ij} + 2G \epsilon_{ij} - \alpha P, \tag{14}$$

where the constants G and λ are called the Lamé constants, p is the pore pressure, and the parameter α (≤ 1) is the Biot’s coefficient, which depends on the compressibility of the constituents and can be defined as

$$\alpha = 1 - \frac{K'}{K_S}. \tag{15}$$

Based on the theory presented above, the static stress equilibrium equation, the Cauchy strain tensor equation, and the constitutive stress–strain relation, the equation of fluid flow in a deformed medium can be written in the displacement form as follows:

$$(\lambda + G) \cdot u_{j,ji} + Gu_{i,jj} + f_i - \alpha P_i = 0. \tag{16}$$

2.3 Characterization of Heterogeneity

Rock is a heterogeneous material, and it is this heterogeneity that causes the stressed rock to fracture via the formation, extension, and coalescence of microcracks in rock. In the absence of heterogeneity, no damage localization occurs and the local behavior of the homogenous model is replicated at the macroscopic scale. Thus, it is necessary to introduce heterogeneity to obtain a collective macroscopic behavior different from that of the individual elements. Heterogeneity is also a key factor that influences material failure forecasting (Vasseur et al. 2015, 2017). To reflect the material heterogeneity at the mesoscale, the mechanical parameters (e.g., strength and Young’s modulus) of the mesoscopic material elements, which are assumed to be homogeneous and isotropic, are assigned randomly using a 2-parameter Weibull statistical distribution (Weibull 1951), as defined in the following statistical probability density function:

$$\varphi(u) = \chi/u_0 (u/u_0)^{\chi-1} \exp\left(- (u/u_0)^\chi\right), \tag{17}$$

where u is the scale parameter of an individual element such as the strength or Young’s modulus and the scale parameter u_0 is related to the average element parameter. The shape parameter χ is larger than zero and reflects the degree of material homogeneity. This shape parameter is called the “homogeneity index”. According to the Weibull distribution,

and the definition of homogeneity index as shown in Fig. 1, a larger χ implies that more elements will have the mechanical properties similar to the mean value, resulting in a more homogeneous material. An extremely high shape parameter χ yields a Gaussian distribution with high kurtosis. The

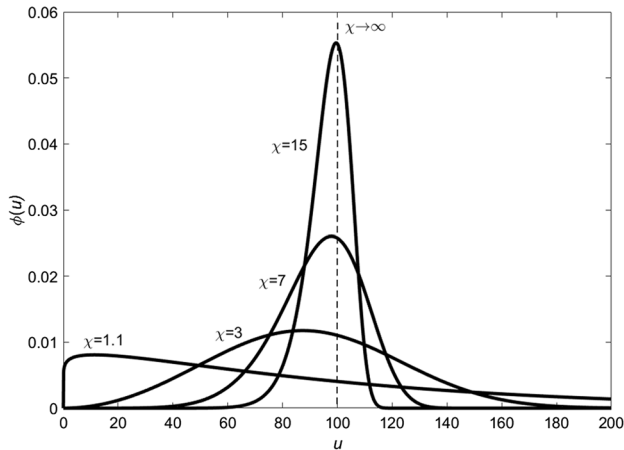


Fig. 1 Distribution density function of parameters of elements with different homogeneity indices of 1.1, 3, 7, and 15 at a given scale parameter of $u_0 = 100$. The scale parameter u approaches to the given average element parameter $u_0 = 100$ when the homogeneity index χ tends to infinity

scale parameter u approaches the average element parameter u_0 when the shape parameter χ tends to infinity.

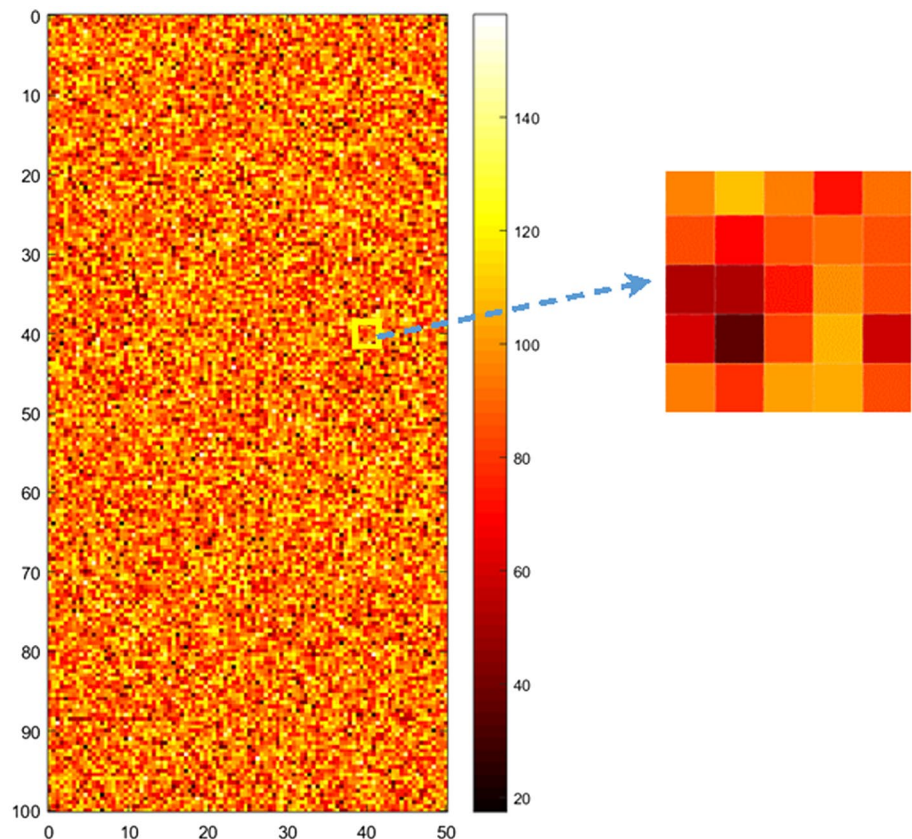
To obtain a set of values of uniaxial compressive strength and Young’s modulus conforming to the Weibull statistical distribution, a set of random numbers ω_i ranging from 0 to 1 are generated according to the Monte Carlo method, and then the uniaxial compressive strength and Young’s modulus of each element can be obtained from

$$u_i = u_0 \ln (1/(1 - \omega_i))^{\frac{1}{\chi}}, \tag{18}$$

where u_i is the uniaxial compressive strength, and u_0 is the average uniaxial compressive strength and Young’s modulus of the element i .

By randomly specifying a uniaxial compressive strength and Young’s modulus to each of the elements, which follows the Weibull distribution according to Eq. (18), a heterogeneous numerical sample can be created. Figure 2 shows a numerical rock sample of 100×50 mm with a homogeneity index of 5 composed of 20,000 (200×100) square elements, produced randomly according to the Weibull distribution and using the uniaxial compressive strength scale parameter 100 MPa. The different brightness in Fig. 2 correspond to different values of element strength (in MPa). The homogeneity index is therefore an important parameter in controlling the macroscopic response of a numerical sample.

Fig. 2 Numerically generated rock specimen with a geometry of 100×50 mm at a given average uniaxial compressive strength of 100 MPa and at a homogeneity index of $\chi = 5$



2.4 Damage Evolution Description

In the model, the system is analyzed at the mesoscale and an elastic damage constitutive law describes its stress–strain relationship. Continuum damage mechanics can describe the effects of progressive microcracking, void nucleation, and microcrack growth at high stress levels using a constitutive law, by making use of a set of state variables that modify the material behavior at the macroscopic level. Using an isotropic continuum damage formulation, the elastic modulus for an isotropic and elastic medium at instantaneous loading can be written as (Lemaitre and Desmorat 2005)

$$E = E_0(1 - D), \tag{19}$$

where ϵ_{ij} is the damaged elastic strain tensor, σ_{ij} is the stress tensor, E and E_0 are the Young’s moduli of the damaged and the undamaged material, respectively, D is the isotropic damage variable, ν is the Poisson’s ratio and δ_{ij} is the Kronecker symbol. In the case of a uniaxial state of stress ($\sigma_{11} \neq 0, \sigma_{22} = \sigma_{33} = 0$), the constitutive relation can be rewritten in terms of the longitudinal stress and strain components only

$$\sigma_{11} = E_0(1 - D)\epsilon_{11}. \tag{20}$$

Hence, for uniaxial loading, the constitutive law is explicitly dependent on damage index D .

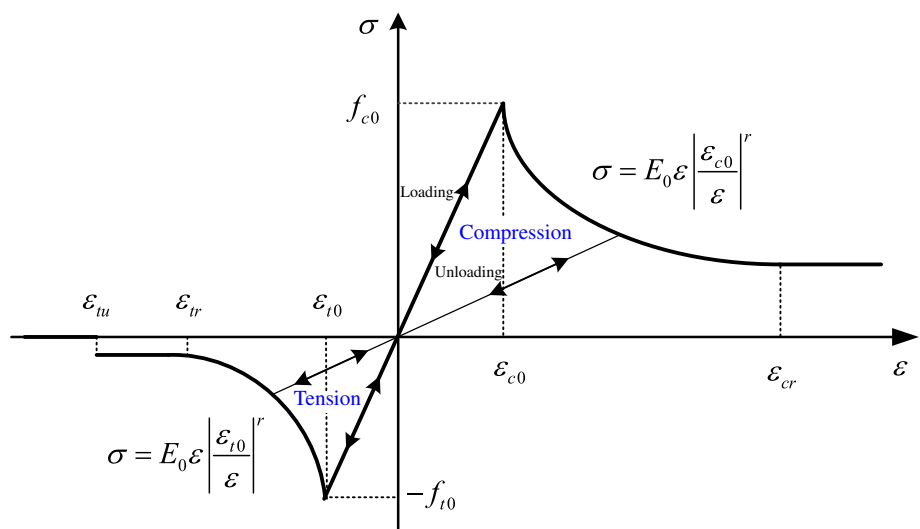
The model used herein is based on progressive isotropic elastic damage. Although other modeling approaches exist that use viscoplastic (e.g., Zhu and Cescotto 1995; Pellet et al. 2005; Sterpi and Gioda 2009) and hydraulic damage (e.g., Karrech et al. 2014) approaches to describe damage accumulation, we highlight here that elastic damage models have been very successful in capturing the brittle behavior of rocks. In the elastic damage model employed here, when

the stress on an element exceeds a damage threshold, its Young’s modulus E is modified according to Eq. (20). Prior to deformation, each element is considered to be elastic, defined by a specific Young’s modulus and Poisson’s ratio. The stress–strain curves of the elements are considered linear elastic until the given damage threshold is reached, followed by strain softening with a constant residual strength. The elastic damage constitutive law of each element under uniaxial stress condition is illustrated in Fig. 3 (Zhu et al. 2014). As stated above, the stress–strain curve of each element is considered linear elastic until the attainment of a given damage threshold. The damage thresholds, the maximum tensile stress criterion and the modified Mohr–Coulomb criterion are used to judge the tensile damage and shear damage of elements, respectively, and are expressed as follows:

$$F_1 = -\sigma_3 - f_{t0} = 0 \quad \text{and} \quad F_2 = \sigma_1 - \sigma_3 \frac{1 + \sin \phi}{1 - \sin \phi} - f_{c0} = 0, \tag{21}$$

where σ_1 and σ_3 are the maximum and minimum principal stresses, respectively, f_{c0} is the uniaxial compressive strength, ϕ is the internal friction angle of the element, f_{t0} is the uniaxial tensile strength, and F_1 and F_2 are the two damage threshold functions. At a given deformation or loading level, the maximum tensile stress criterion is always checked first with priority to judge whether the element is damaged (since, as discussed above, rock is far weaker in tension than in compression). If the element is not damaged in tension, the Mohr–Coulomb criterion is then used to judge whether the element is damaged in shear. The sign convention used throughout this paper is that compressive stresses and strains are positive and tensile stresses and strains are negative.

Fig. 3 Elastic compressive and tensile damage constitutive relations of an element. Each element with a randomly assigned mechanical properties conforming to statistical Weibull distribution in the numerically generated specimen possesses the elastic compressive and tensile damage constitutive relation



According to the constitutive law as shown in Fig. 3, the damage variable D can be described as follows:

$$D = \begin{cases} 0, & F_1 < 0 \text{ and } F_2 < 0, \\ 1 - (\varepsilon_{t0}/\varepsilon_3)^r, & F_1 = 0 \text{ and } dF_1 > 0 \\ 1 - (\varepsilon_{c0}/\varepsilon_1)^r, & F_2 = 0 \text{ and } dF_2 > 0, \end{cases} \quad (22)$$

where ε_1 and ε_3 are the major principal strain and minor principal strain, respectively. ε_{t0} is the uniaxial tensile strain at the elastic limit in tension and $\varepsilon_{t0} = f_{t0}/E_0$, and ε_{c0} is the uniaxial compressive strain at the elastic limit in compression and $\varepsilon_{c0} = f_{c0}/E_0$, and the exponent r is a constitutive coefficient with a value of 2.0.

Specifically, the damage variable D of the elements in tension can be expressed as

$$D = \begin{cases} 0, & \varepsilon > \varepsilon_{t0}, \\ 1 - (\varepsilon_{t0}/\varepsilon)^r, & \varepsilon_{tr} < \varepsilon \leq \varepsilon_{t0}, \\ 1 - \zeta \varepsilon_{t0}/\varepsilon, & \varepsilon_{tu} \leq \varepsilon \leq \varepsilon_{tr}, \\ 1 & \varepsilon < \varepsilon_{tu}, \end{cases} \quad (23)$$

where ε_{t0} is the uniaxial tensile strain at the elastic limit in tension (also called threshold strain) and $\varepsilon_{t0} = f_{t0}/E_0$, ζ is the residual strength coefficient and $\zeta = f_{tr}/f_{t0} = (\varepsilon_{t0}/\varepsilon_{tr})^{(r-1)}$, and f_{tr} is the uniaxial residual tensile strength in tension and ε_{tr} is the corresponding strain at residual tensile strength in tension, ε_{tu} is the ultimate tensile strain corresponding to the completely damaged state (i.e., failure at $D=1$) of an element. The ultimate tensile strain coefficient $\eta = \varepsilon_{tu}/\varepsilon_{tr}$ is introduced in our model and is set to 5 by default. The exponent r is a constitutive coefficient with a value of 2.0.

The damage variable D of the elements in compression can be expressed as

$$D = \begin{cases} 0, & \varepsilon \leq \varepsilon_{c0}, \\ 1 - (\varepsilon_{c0}/\varepsilon)^r, & \varepsilon_{c0} < \varepsilon \leq \varepsilon_{cr} \\ 1 - \zeta \varepsilon_{c0}/\varepsilon, & \varepsilon > \varepsilon_{cr}, \end{cases} \quad (24)$$

where ε_{c0} is the uniaxial compressive strain at the elastic limit in compression and $\varepsilon_{c0} = f_{c0}/E_0$, ζ is the residual strength coefficient and $\zeta = f_{cr}/f_{c0} = (\varepsilon_{c0}/\varepsilon_{cr})^{(r-1)}$, and ε_{cr} is the ultimate residual compressive strain and $\varepsilon_{cr} = \zeta^{r-1} \varepsilon_{c0}$.

In this respect, the damage variable calculated with Eqs. (23) and (24) is always from zero to one regardless of the type of damage (tensile or shear). We should note that the occurrence of damage should not be confused with the initiation of cracks. The elements whose ultimate tensile strains are attained can only “crack” within a width of the element. That is to say, cracking is coincident with complete damage or failure. Shear-induced damage will not lead to the occurrence of cracks but the degradation of elements. Using this method, the initiation, growth and coalescence of cracks

can be easily reproduced. Furthermore, in the damage zone, to distinctly display the two kinds of damage modes (i.e., tensile damage and shear damage) in the post-processing figures, the tensile damage is represented as negative numbers, while the shear damage is represented as positive ones. During the numerical implementation of the above equations with finite element analysis, Eq. (21) was used as a damage criterion to check the stress conditions calculated with Eqs. (4) and (10) to judge if damage occurs. Thus, Eq. (22) was used to calculate the damage variable D . If any of the elements in a stressed specimen are damaged, the damaged elements will undergo a degradation of their elastic modulus according to the elastic damage constitutive relationship.

In this model, $D=1$ corresponds to the complete damage or failure of the element, and the elastic modulus of this element tends to zero. To avoid possible instability in finite element analysis, a small decimal (1.0×10^{-5} MPa by default) is given to the elastic modulus of a failed element. Correspondingly, the total strain will increase due to the elastic modulus degradation with increasing time. When damaged or failed elements are clustered, it may lead to the macroscopic failure of the specimen. Therefore, although the Eq. (22) is time-independent, it is capable of describing the time-dependent evolution of damage when it is coupled with the creep model as given in Eq. (10) to describe the creep behavior of rock.

AEs are transient elastic waves generated by the rapid release of energy within a material, such as the strain energy released during microcrack propagation. Monitoring AE during deformation has become an increasingly important diagnostic tool in material science and has provided a wealth of information regarding the failure process in brittle materials. AE monitoring has shed light on the onset of microcracking during deformation (Wong et al. 1997), the evolution the spatial and temporal progression of microcracks (Ohnaka 1983; Lockner 1993a, b; Fortin et al. 2009; Aker et al. 2014), amongst many more. For instance, Lockner (1993a, b) analyzed catalogs of AE events recorded during compressive loading tests on rock. The AE events were analyzed in terms of the information they offer about the accumulated state of damage in a material. This measured damage state can be combined with a model for the weakening behavior of cracked solids, showing that reasonable predictions of the mechanical behavior are possible. Based on this prior knowledge, it is reasonable to assume that the number of AE events is proportional to the number of damaged elements and that the strain energy released (the strain energy before and after damage) corresponds to the energy of that particular AE event (Tang 1997). In our model, we can use the output of AE to indirectly assess the damage evolution. However, it must be mentioned that aseismic damage during rock creep tests could possibly occur. The causes of aseismic damage are numerous, for example, the low surface energy

of calcite, radiated energy being absorbed by neighboring dislocation, and/or intermittent dislocation flow (Weiss and Marsan 2003; Schubnel et al. 2006), amongst many more. Indeed, an experimental study showed that pressure solution creep is an important mechanism in the time-dependent behavior of porous limestone (Brantut et al. 2014b).

Although the assumption that the number of AE events is proportional to the number of damaged elements and that the strain energy released corresponds to the energy of that particular AE event is obviously a simplification of what occurs in reality, it has been shown that this micromechanical representation of microcracking can yield realistic patterns and can reproduce the macromechanical behavior of heterogeneous rock. In our model, by recording the number of failed elements and calculating the elastic energy released from the failed elements, the AE counts and AE energy associated with the progressive failure of the material can be simulated (Xu et al. 2017).

In the numerical code, the numerical model is loaded either in a displacement control mode (i.e., constant displacement rate) or in a load control mode (i.e., constant stress). At each loading or time increment, the stress and strain and the stress field and flow field are examined and those elements that are strained beyond the pre-defined strength threshold are broken irreversibly. The stiffness and strength of an element is reduced if it is broken, as discussed above. If some elements fail, then the model, now containing new parameters for some of its elements, moves to a new equilibrium. The next load or time increment is added only when there are no more elements strained beyond the strength threshold at an equilibrium strain field. Thus, numerical loading in the model is similar to that of deformation experiments performed in the laboratory.

3 Implementation of Numerical Model

The modeling approach described above requires that both the damage state and the damage-induced modification of elastic stiffness in brittle rocks are continually updated. Consequently, the problem is non-linear and an iterative numerical procedure is therefore implemented that is based on the finite element method. A flow chart of the model is shown in Fig. 4 to clarify the implementation of the numerical model. The procedure outlined in Fig. 4 was first performed in MATLAB to define the evolution of the damage constitutive parameters and then implemented into the finite element model COMSOL Multiphysics to define the spatial behavior.

A point worth emphasizing here is that the proposed model needs to be calibrated with experimental data to determine the appropriate input parameters. In principle, a complete calibration process must be undertaken at both the mesoscale and the macroscale. At the mesoscale, the

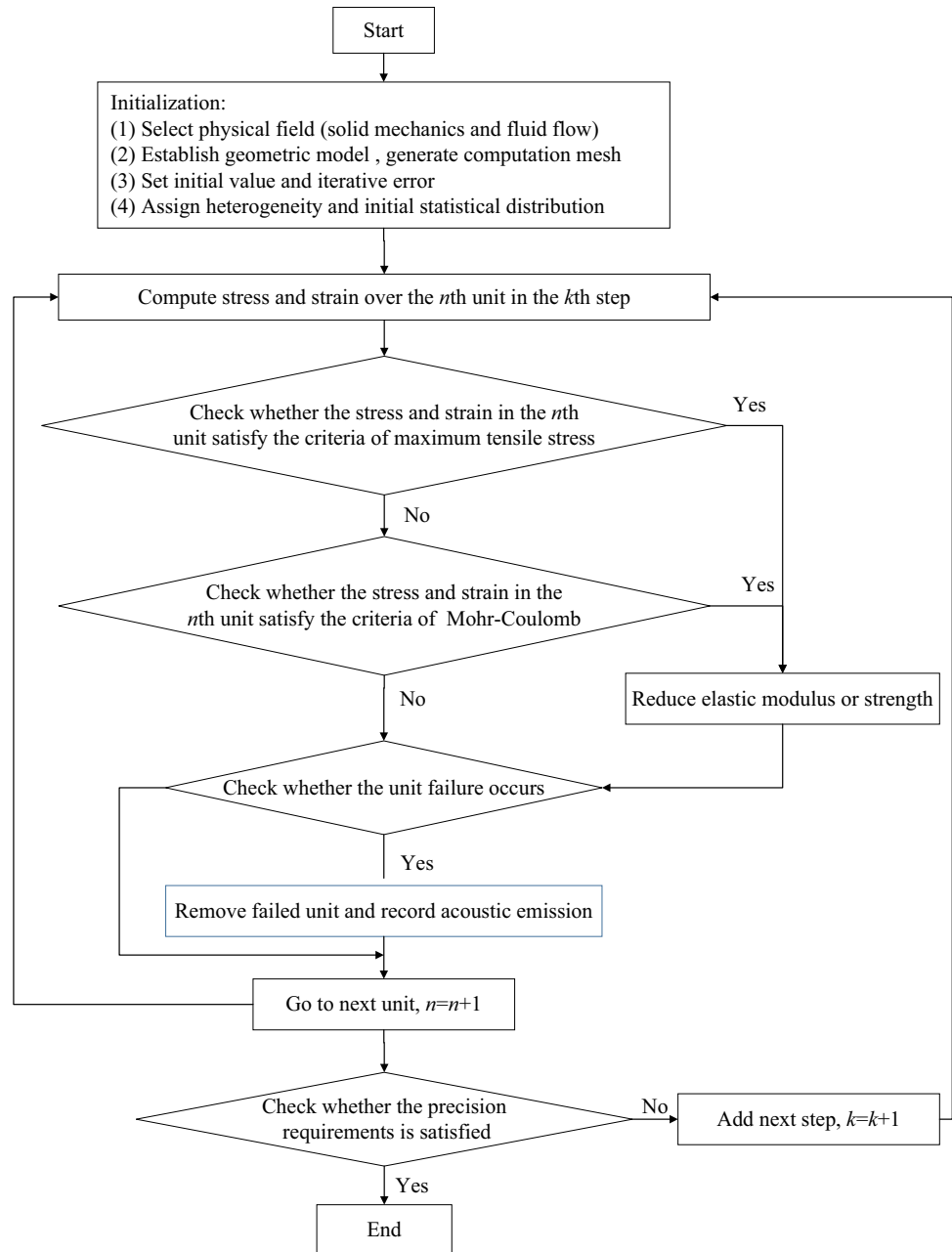
behaviors of the representative elemental volume (REV) are governed by the initial microstructural parameters, the damage-based constitutive law, and the failure criterion of the REV. It is straightforward to obtain accurate parameters to represent the initial mesoscale structures in the REV from mesoscopic observations, but the calibration of the damage constitutive law and the failure criterion at the mesoscale is more challenging—principally due to the difficulties in performing direct mechanical tests on the REV. An approximate method is the utilization of macroscopic standard laboratory tests instead of mesoscopic tests (Homand-Etienne et al. 1998). However, the development of novel experiments at the mesoscale of the REV is needed to further improve the model calibration at the mesoscale. With the calibrated mesoscale parameters defined, then the macroscopic numerical model can be calibrated from conventional constant strain rate tests and creep tests on standard rock samples to determine the parameters of heterogeneity and the REV size. After the full calibration of the proposed model, it can be used to predict the time-dependent deformation and fracturing behavior of brittle rocks at elevated pore pressure and under external loading.

Currently, a few calibration studies—partially related to our proposed model—have been performed on different types of rocks (Golshani et al. 2006; Wong et al. 2006). The input model parameters chosen herein were selected by referring to these calibrated parameters. However, further studies must explore a more accurate and rigorous method for model calibration that includes new experiments conducted on the same rock type at both the mesoscale and the macroscale. In the following section, the model is first validated against previously published experimental data to obtain the input parameters of the simulations. Our model is then used to simulate the time-dependent brittle creep behavior (constant external loading) of rocks under various constant pore and confining pressures.

4 Validation of the Model

Before we can investigate the influence of various parameters (such as pore pressure, confining pressure, and sample homogeneity) on brittle creep, we must first validate our model using published experimental data on an appropriate experimental material. We use here the experimental data of Yang et al. (2014) on red sandstone. This study includes constant strain rate and brittle creep experiments performed at various constant pore and confining pressures. The high permeability of the red sandstone used in Yang et al. (2014) ensured drained conditions over the range of strain rates used. Therefore, our simulations are set such that the boundary conditions ensure drained conditions (i.e., the pore pressure does not change during the deformation of the sample).

Fig. 4 Flow chart of the coupled hydro-mechanical time-dependent model



4.1 Constant Strain Rate Tests on Sandstone Under Confining and Pore Pressures

A series of constant displacement rate experiments (i.e., conventional confined compressive strength experiments) were numerically conducted to obtain the input parameters at the mesoscale from the macroscopic physico-mechanical properties of our studied rock. The macroscopic mechanical properties of red sandstone have been investigated and described previously (Yang et al. 2014). The connected porosity of tested red sandstone is approximately 8.6%. All the experiments of Yang et al. (2014) were performed at room temperature. The geometry of the cylindrical sandstone

samples in laboratory was 100 mm in length and 50 mm in diameter. The compressive strength of red sandstone under confining pressures of 5, 10, 20, and 30 MPa was measured to be 132, 162, 228, and 252 MPa, respectively (Yang et al. 2014). The Young's modulus and Poisson's ratio of red sandstone in uniaxial compression are 20 MPa and 0.25, respectively. Similar to the experimental tests in laboratory, numerical specimens with 100 mm in length and 50 mm in width were randomly generated and were discretized into 200×100 (20,000 elements) square elements (i.e., each square element had sides of 0.5 mm). The dimensions of the two-dimensional modeled sample were kept the same for all of the numerical simulations throughout this paper. A suite

of prescribed displacement increments was applied to both ends of the modeled rock samples at constant confining pressures of 5, 10, 20, and 30 MPa (pore pressure = 0 MPa). The physico-mechanical input parameters of the individual elements at the mesoscale used in the simulations were determined by trial and error according to the experimental data

(the determined parameters are listed in Table 1). It is noted that the input parameters for the elements at the mesoscale listed in Table 1 represent the statistical mechanical properties of the sandstone specimen at a macroscale.

Figure 5 presents the numerical stress–strain curves of dry red sandstone specimens deformed at confining pressures of 5, 10, 20, and 30 MPa (pore pressure = 0 MPa), together with the experimental stress–strain curves (Yang et al. 2014). The compressive strength of sandstone samples increases with each increase in confining pressure. We highlight that the simulated stress–strain curves are in reasonable agreement with the experimental stress–strain curves (Fig. 5). It is again highlighted that the model input parameters were the same for each of the simulations shown in Fig. 5 (Table 1), adding confidence that our model is capable of accurately capturing the short-term mechanical behavior of sandstone under different confining pressures.

Table 1 Physico-mechanical parameters of numerical model

Items	Specimen
Homogeneity index	5
Mean uniaxial compressive strength (MPa)	280
Mean Young’s modulus (GPa)	20
Poisson ratio	0.25
Ratio of compressive to tensile strength	10
Frictional angle (°)	30

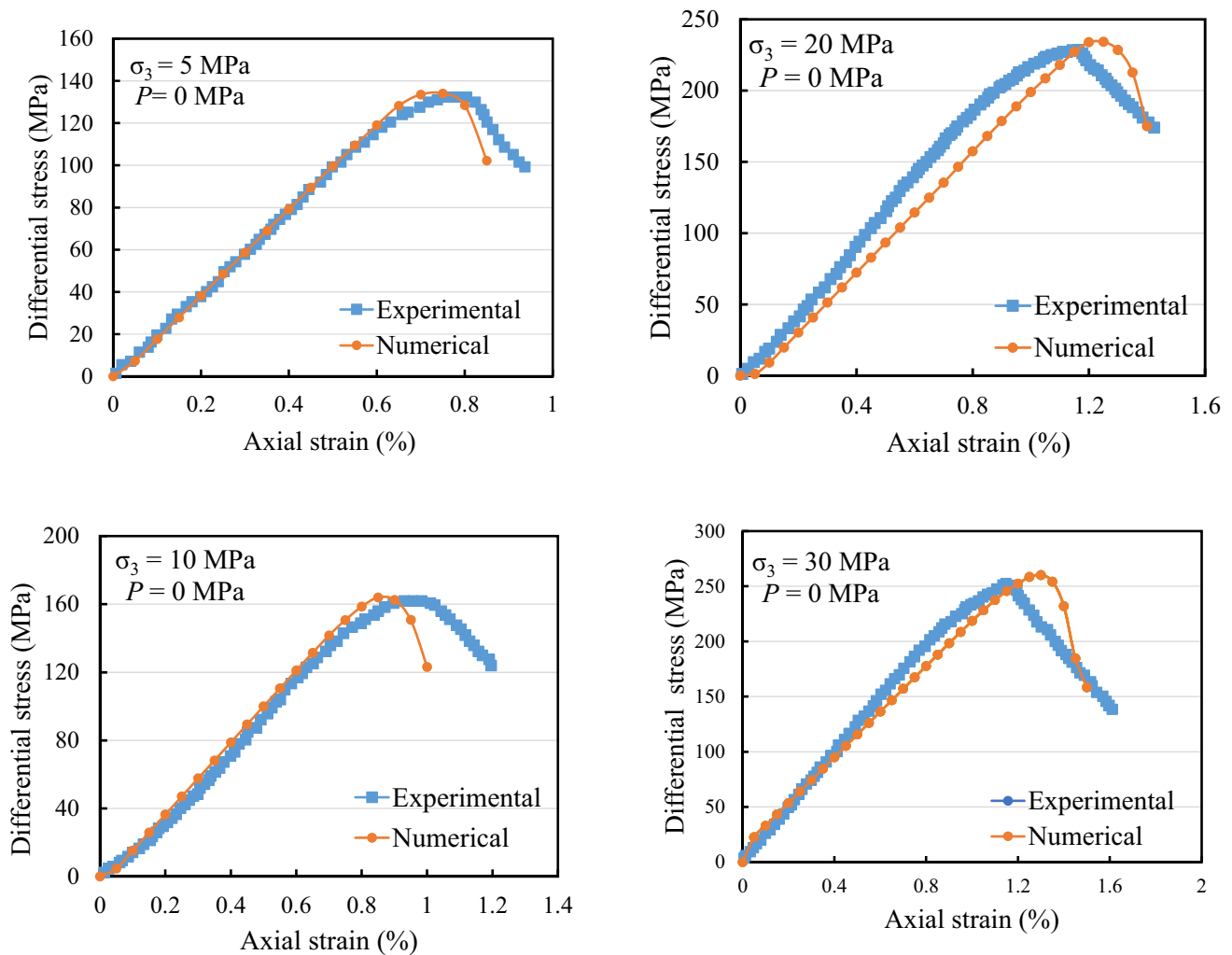


Fig. 5 Comparisons between numerical (orange circles) and experimental (blue squares) stress–strain curves of red sandstone specimens under various confining pressures of 5, 10, 20, and 30 MPa (pore

pressure = 0 MPa). All simulations were performed under the same input parameters except for the confining pressure. Experimental data from Yang et al. (2014). (Colour figure online)

Conventional triaxial compressive tests on the saturated red sandstone samples deformed under the same confining pressure (30 MPa) but various pore pressures (5, 10, and 15 MPa) were also performed in the laboratory (Yang et al. 2014). Assuming a simple effective pressure law, these conditions correspond to effective pressures of 25, 20, and 15 MPa, respectively. We performed numerical simulations under the same experimental conditions. The physico-mechanical input parameters of the individual elements at the mesoscale used in these simulations are kept the same (listed in Table 1). The numerical stress–strain curves of the sandstone specimens at a confining pressure of 30 MPa and pore pressures of 5, 10, and 15 MPa, together with the experimental stress–strain curves of Yang et al. (2014), are presented in Fig. 6. We find that the compressive strength of sandstone samples decreases with an increase in pore pressure at a given confining pressure (i.e., a reduction in effective pressure), and that the simulated stress–strain curves are in reasonable agreement with the experimental stress–strain curves.

It is typically observed that the effective pressure (defined here as the confining pressure minus the pore pressure multiplied by a poroelastic coefficient) usually controls stress–strain and strength behavior in rock, independent of the magnitude of the pore pressure. Thus, we performed two additional tests on sandstone specimens under the same effective pressure to evaluate the applicability of effective pressure principle in our model. One sandstone specimen was deformed under a confining pressure of 24 MPa without pore pressure (i.e., effective pressure = 24 MPa), and another sandstone specimen was deformed under a confining pressure of 34 MPa and a pore pressure of 10 MPa (i.e., effective pressure = 24 MPa). Figure 7 shows the experimental stress–strain curves of the sandstone specimens under the same effective pressure, together with the modeled curves. We notice that the peak stress of the two sandstone specimens is almost identical under the same effective pressure (Fig. 7). It is well known that the coefficient of pore pressure is an important component of the effective pressure law. Some existing studies (She and Xuan 2010; Baud et al. 2015; Farquharson et al. 2016) have shown that the pore pressure coefficient is close to but less than one. Thus, the coefficient of pore pressure was set to one in the numerical simulations performed in this study. We highlight that the numerical and experimental stress–strain curves under the same effective pressure, as shown in Fig. 7, are in very good agreement.

From the simulated mechanical behavior of sandstone specimens under various pressure conditions (Figs. 5, 6, 7), we can arrive at the conclusion that the proposed model is capable of capturing the short-term (time-independent) mechanical behavior of porous sandstone.

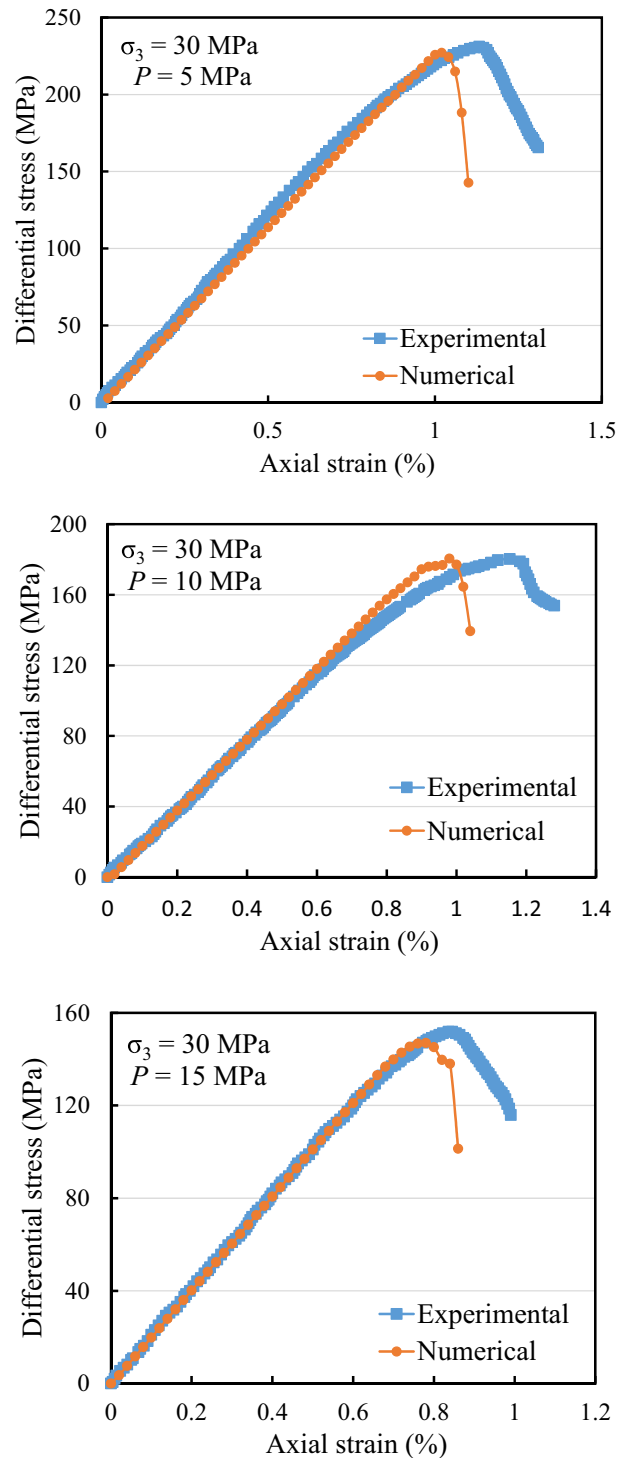


Fig. 6 Comparisons between numerical (red lines) and experimental (blue lines) stress–strain curves at constant confining pressures of 30 MPa and various constant pore pressures of 5, 10, and 15 MPa (i.e., effective pressures of 25, 20, and 15 MPa, respectively). All simulations were performed under the same input parameters except for the pore pressure. Experimental data from Yang et al. (2014). (Colour figure online)

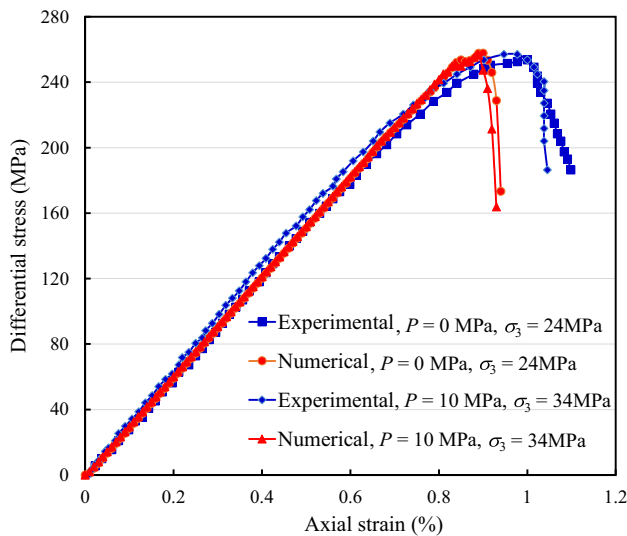


Fig. 7 Comparisons between numerical (orange circles) and experimental (blue squares) stress–strain curves of red sandstone specimens under the same effective pressures. All simulations were performed under the same input parameters except for the confining and pore pressures. Experimental data from Yang et al. (2014). (Colour figure online)

4.2 Brittle Creep Tests on Sandstone Under Confining and Pore Pressures

As described above, the validity of our numerical model was tested by trying to replicate experimental data from triaxial deformation experiments on sandstone under different constant confining and pore pressures. The proposed model will now be used to simulate a suite of conventional brittle creep experiments under a constant confining pressure of 30 MPa and at different constant pore pressures of 5, 10, and 15 MPa (i.e., effective pressures of 25, 20, and 15 MPa). The numerical creep simulations were all performed using the determined physico-mechanical parameters listed in Table 1. In addition to the constant strain rate experiments described above, to simulate coupled hydro-mechanical time-dependent behavior, hydro-physical parameters such as permeability, and dynamic viscosity, as well as the material constants A , m , and n are also needed. Based on the experimental data on the macroscopic physico-mechanical properties of rocks and the statistical distribution relationship between the physico-mechanical properties of the elements at the mesoscale and the physico-mechanical properties of rocks at a macroscale, the input parameters for physico-mechanical properties of the elements at the mesoscale can be determined by an inverse analysis method. Thus, these hydro-physical parameters such as permeability and dynamic viscosity are determined from the experimental data (Yang et al. 2014) and material constants A , m , and n can also be determined using a fitting method. All input parameters for

Table 2 Physico-mechanical parameters of numerical model for sandstone

Parameters	Values
Homogeneity index (χ)	5
Mean Young' modulus (GPa)	20
Mean UCS (MPa)	280
Poisson ratio	0.25
Ratio of compressive to tensile strength	10
Frictional angle ($^\circ$)	30
Permeability (m^2)	1×10^{-18}
Dynamic viscosity (Pa s)	1×10^{-3}
A	5×10^{-11}
n	1.65
m	0.6
U	5000

the numerical model are listed in Table 2. During the simulations, the elements at the bottom of the modeled rock sample are fixed in the vertical direction but they can move freely in the horizontal direction, as is the case for conventional triaxial compressive loading in the laboratory (i.e., the elements cannot move into the piston/baseplate).

The numerical simulated creep curves (axial strain vs. time), together with the experimental curves (from Yang et al. 2014), are plotted in Fig. 8. The experiments, and therefore simulations, were performed at constant differential stresses of 142, 160, and 180 MPa for the experiments/simulations at effective pressures of 15, 20, and 25 MPa, respectively. It can be seen from Fig. 8 that the numerically simulated creep curves are in good agreement with the experimental curves. The numerical creep curves produced by our model clearly show the decelerating–accelerating phenomenology of brittle creep seen in laboratory experiments (see the review by Brantut et al. 2013). In particular, the increase in axial strain rate preceding sample failure is well reproduced by the proposed model. We therefore conclude that, based on these validations, our model can be used to investigate the hydro-mechanical time-dependent creep response of inhomogeneous brittle rocks under different pore and confining pressures.

Figure 9 shows several snapshots of the damage evolution of numerical specimens for the three creep simulations performed at effective pressures of 15, 20, and 25 MPa. These images clearly show when and where the damage and failure occur in the rock specimen. Due to the heterogeneity of rock specimen, the elastic moduli for the elements in the rock sample at the mesoscale are spatially distributed at random. Elements with a low strength and elastic modulus are damaged first. As time goes on, the number of damaged elements continued to grow, forming discrete damage zones. These local damaged zones modify the stress field in

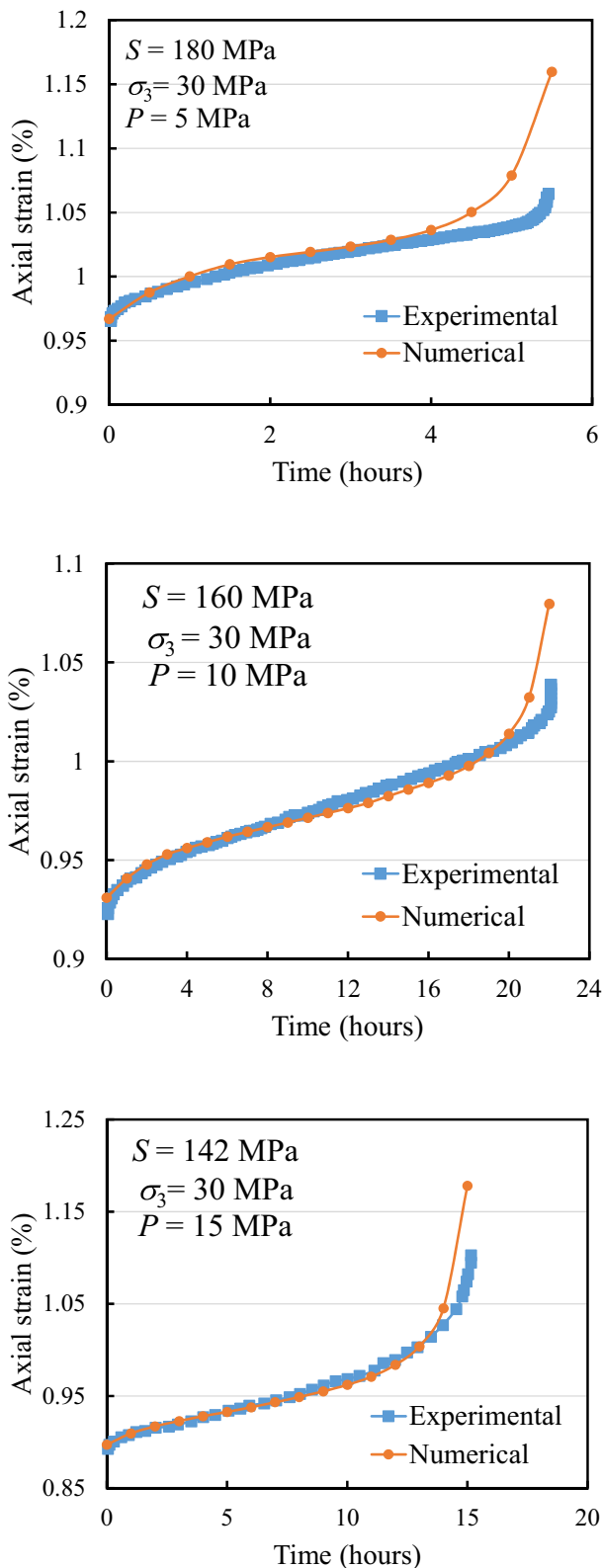


Fig. 8 Comparisons between numerical (orange circles) and experimental (blue squares) creep curves at various constant effective pressures of 25, 20, and 15 MPa (confining pressure = 30 MPa, pore pressure = 5, 10, and 15 MPa, respectively). All simulations were performed under the same input parameters except for the pore pressure and differential stress. (Colour figure online)

their surrounding region and these modifications trigger the dynamic extension of damage into neighboring elements. Furthermore, we find that formation of the damage zone that ultimately results in sample failure initiates during the accelerating portion of the creep curve.

Since our simulations accurately capture the decelerating–accelerating nature of a classic experimental creep curve (Fig. 8), we therefore conclude that, based on these validations, our time-dependent model can be used to investigate the hydro-mechanical time-dependent brittle response of inhomogeneous brittle rock under different effective pressures and applied differential stresses.

5 Numerical Simulations and Discussion

5.1 Model Setup

In this section, we use the proposed model to further investigate the influence of effective pressure, differential stress, and sample heterogeneity on brittle creep of rock. The numerical samples used in these simulations have a geometry of 100×50 mm (Fig. 10). The sample size is therefore the same as the samples modeled in the above-described validation. The geometry of the modeled sample was discretized into a 200×100 (20,000 elements) square grid (i.e., each square element had sides of 0.5 mm). We will apply various axial differential stresses (138, 140, 142, 144, and 146 MPa) and various constant effective pressures (10, 15, 20, and 25 MPa) on numerical heterogeneous samples ($\chi = 6, 7, \text{ and } 8$) to investigate brittle creep in inhomogeneous rock. The loading and boundary conditions are also shown in Fig. 10. Similar to conventional creep tests, the axial stress (σ_y) was maintained constant at the top of the specimen. At the same time, the sample is subject to a constant confining pressure (σ_x) and pore pressure during the simulations. During the simulations, the elements at the bottom of the modeled rock sample are fixed in the vertical direction but they can move freely in the horizontal direction, as is the case for conventional triaxial compressive creep tests in the laboratory (i.e., the elements cannot move into the piston/baseplate). The relevant model parameters used in the simulations are the same as the parameters listed in Table 2.

5.2 Effect of Effective Pressure

Based on these validations above, four additional numerical creep tests were performed at a differential stress of 142 MPa and at constant effective pressures of 10, 15, 20, and 25 MPa to investigate the effect of effective pressure on the brittle creep of rock. The confining pressure for these simulations was 30 MPa and the pore pressures were 5, 10,

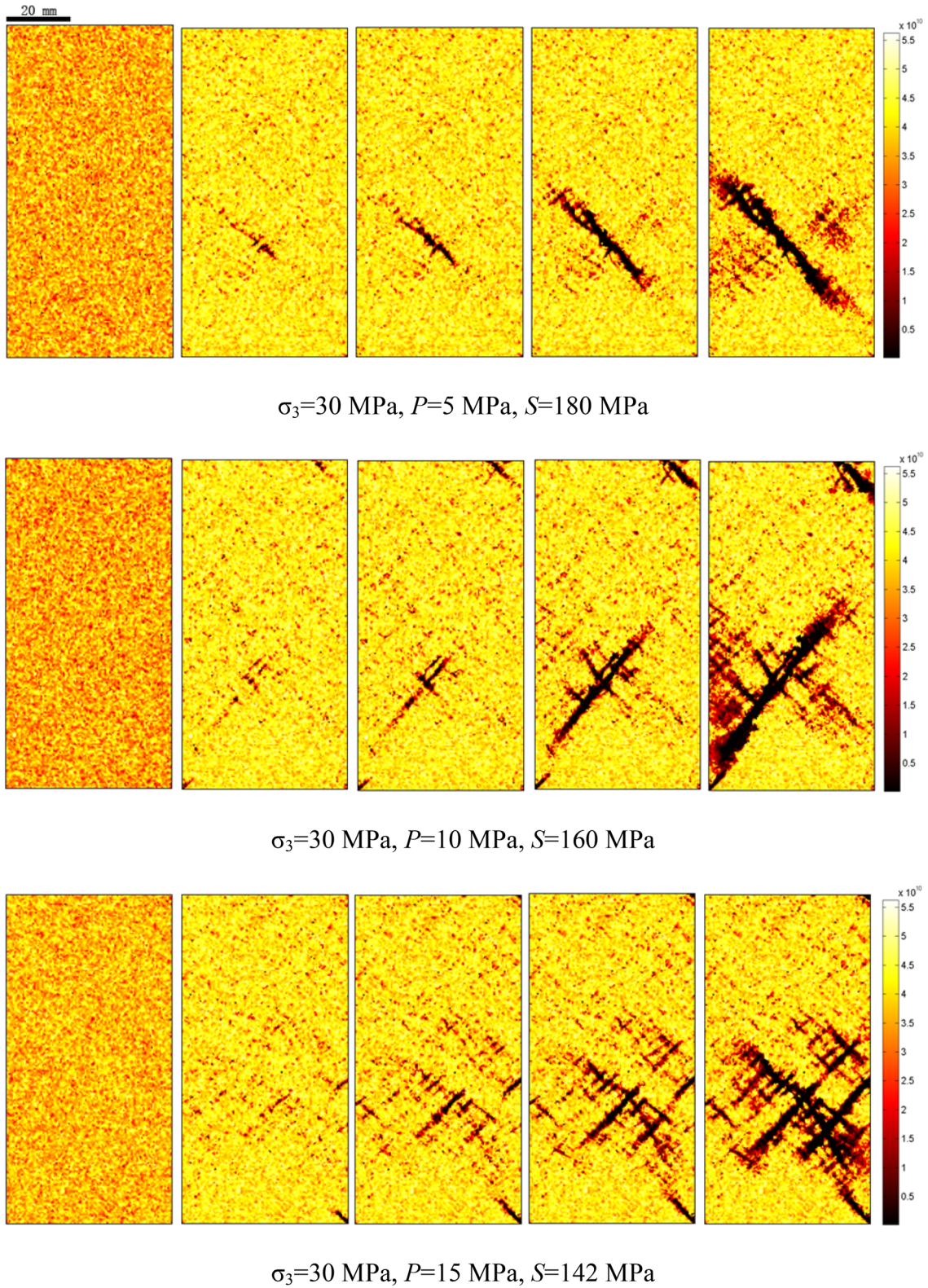


Fig. 9 Damage and failure processes of numerical specimens at various constant effective pressures of 25, 20, and 15 MPa (confining pressure=30 MPa, pore pressure=5, 10, and 15 MPa, respectively).

The dark colors in the numerical specimen are the damage-induced fractures. (Colour figure online)

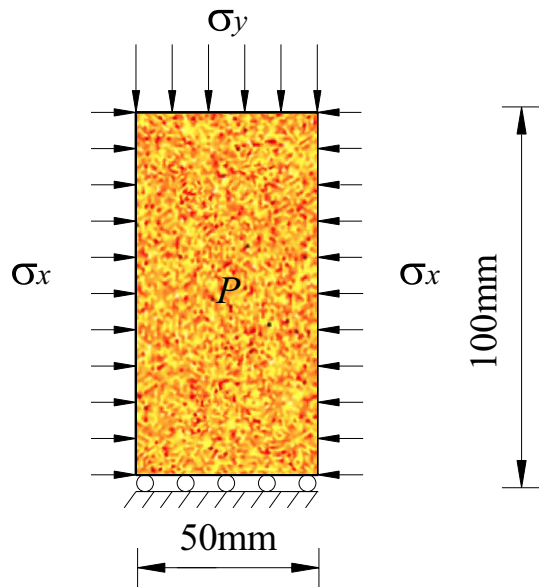


Fig. 10 Numerical model with a geometry of 100 mm in height and 50 mm in width for the confined creep simulations

15, and 20 MPa, respectively. Figure 11 shows the creep curves and AE activity as a function of time for the four constant effective pressures tested (10, 15, 20, and 25 MPa). We can see that all the simulated creep curves exhibit the decelerating–accelerating phenomenology of brittle creep as observed in the laboratory (Brantut et al. 2013). The start of the creep simulations is accompanied by a few AE events, the result of the failure of a few weak elements in numerical sample. With increasing time, the rock samples transition from decelerating to accelerating creep. Interactions among elements during accelerating creep results in strain localization, and ultimately, the macroscopic failure of the sample. The approach to macroscopic failure is accompanied by an acceleration in the AE hit rate (Fig. 11). In general, the creep curves and the output of AE follow a very similar trend.

For comparison, the creep curves for these simulations are plotted together in Fig. 12. We can see that the effective pressure has a marked effect on creep behavior (as observed in experimental studies of, for example, Heap et al. 2009a, 2011; Brantut et al. 2013). For example, the minimum creep strain rate increases as the effective pressure decreases (Fig. 13). The minimum creep strain rate was increased from $\sim 1 \times 10^{-8}$ to $\sim 2\text{--}3 \times 10^{-8} \text{ s}^{-1}$ as the effective

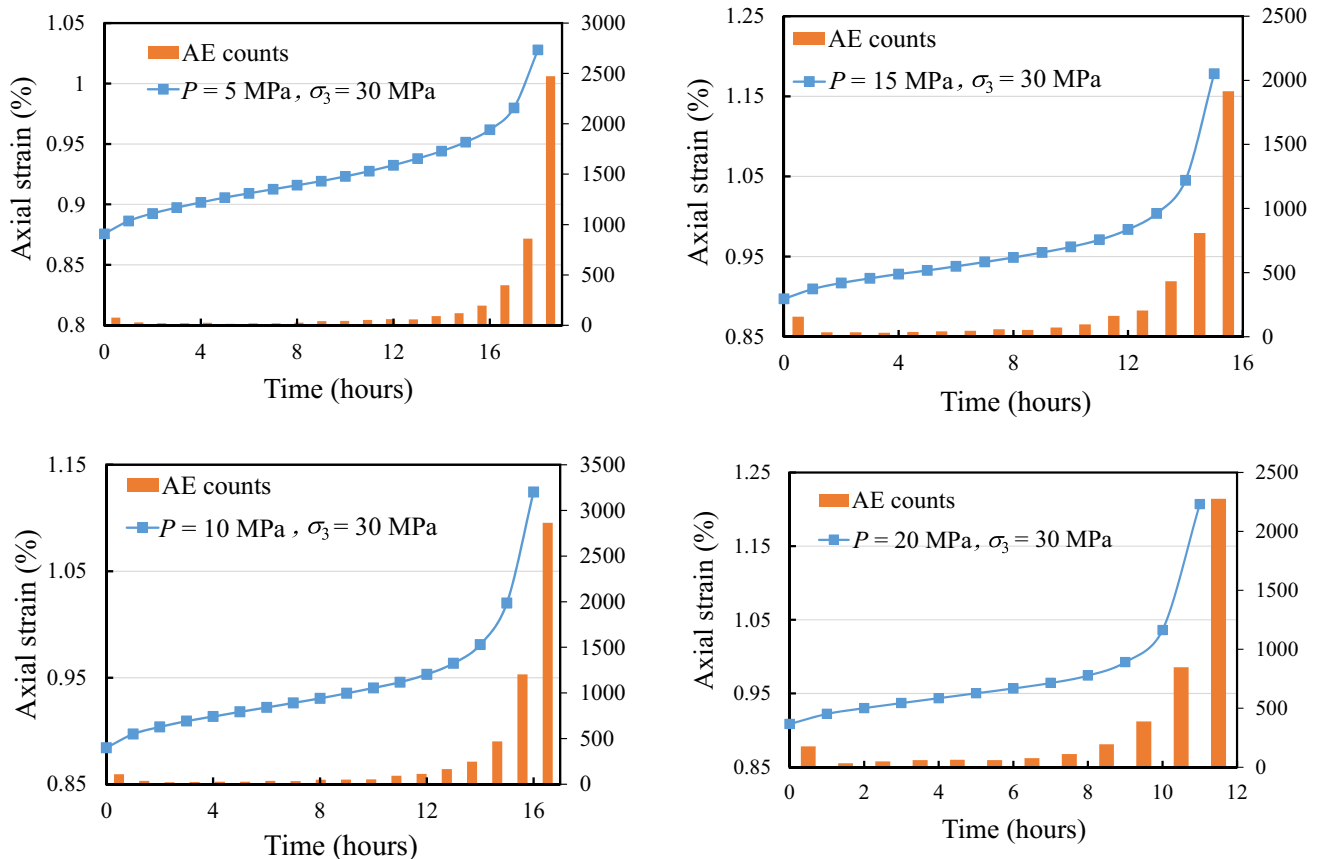


Fig. 11 Creep curves and AE sequences of numerical specimens at various constant effective pressures of 25, 20, 15, and 10 MPa (confining pressure = 30 MPa, pore pressure = 5, 10, 15, and 20 MPa, respectively). All simulations were performed under the same input parameters

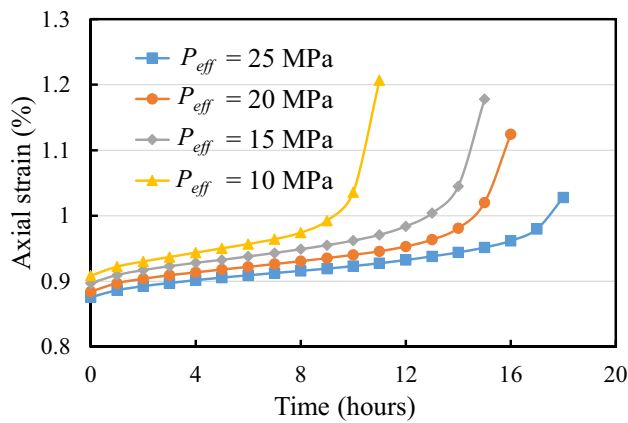


Fig. 12 Creep curves of numerical specimens at various constant effective pressures of 25, 20, 15, and 10 MPa (confining pressure = 30 MPa, pore pressure = 5, 10, 15, and 20 MPa, respectively). All simulations were performed under the same input parameters

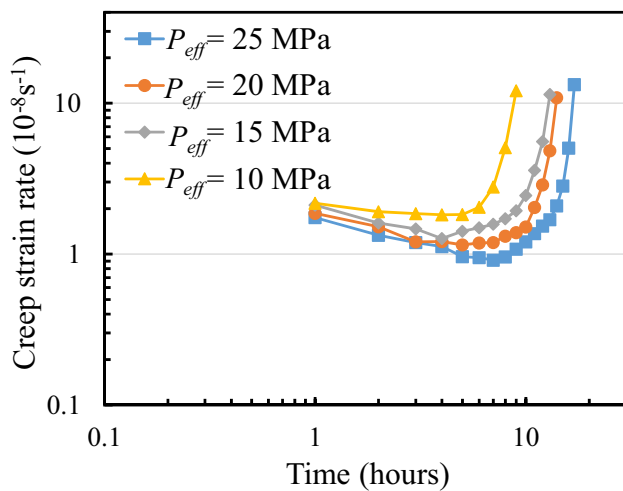


Fig. 13 Simulated creep strain rate versus time curves for numerical specimens deformed at various effective pressures of 25, 20, 15, and 10 MPa (confining pressure = 30 MPa, pore pressure = 5, 10, 15, and 20 MPa, respectively). All simulations were performed under the same input parameters

pressure was reduced from 25 to 10 MPa (Fig. 13). The time-to-failure was also reduced as the effective pressure was reduced (Fig. 14). In detail, time-to-failure was reduced from ~ 19 to ~ 12 h upon reducing the effective pressure from 25 to 10 MPa (Fig. 14).

We also used the proposed model to simulate brittle creep of sandstone samples under different constant confining pressures of 20, 22, 25, 28, and 30 MPa but the same constant pore pressure of 15 MPa (i.e., effective pressures of 5, 7, 10, 13, and 15 MPa) and the same constant applied differential stress of 142 MPa. Figure 15 shows the numerically obtained axial creep strain curves and AE activity with

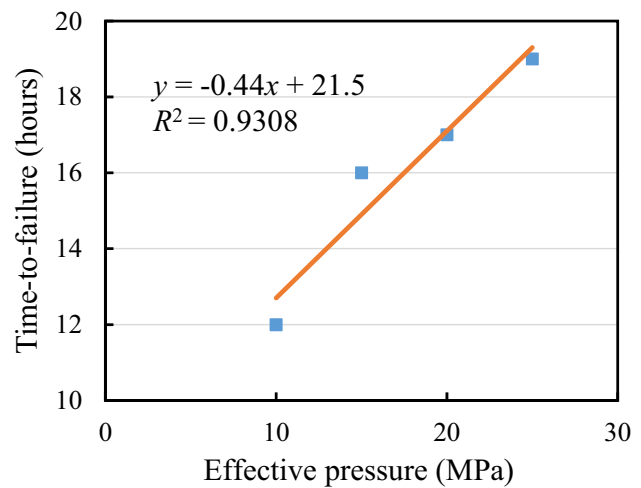


Fig. 14 Simulated time-to-failure versus pore pressure curves of numerical specimens at various constant effective pressures of 25, 20, 15, and 10 MPa (confining pressure = 30 MPa, pore pressure = 5, 10, 15, and 20 MPa, respectively). All simulations were performed under the same input parameters

time for these simulations, and Fig. 16 shows the creep strain rate as a function of time. As for the above-described simulations, the simulations presented in Figs. 15 and 16 show that increasing the effective pressure for a given constant differential stress (1) reduces the creep strain rate and (2) increases the time-to-failure. For example, at an effective pressure of 5 MPa, the sample had a minimum creep strain rate of $\sim 2 \times 10^{-7} \text{ s}^{-1}$ and failed after about 1.75 h, whereas at an effective pressure of 15 MPa, the minimum creep strain rate was reduced to $\sim 2 \times 10^{-8} \text{ s}^{-1}$ and sample failure occurred after about 7.25 h (Figs. 15, 16).

These findings are qualitatively similar to those who have investigated the influence of effective pressure on brittle creep in porous sandstones in the laboratory (e.g., Baud and Meredith 1997; Ngwenya et al. 2001; Heap et al. 2009a; Brantut et al. 2013, 2014a).

5.3 Effect of Differential Stress

We will now run a suite of conventional brittle creep experiments under different constants applied differential stresses (i.e., we changed the ratio between the creep hold stress and the short-term failure stress) to study the effect of differential stress (axial stress minus confining pressure) on creep. We performed creep tests at constant pore pressure of 15 MPa and constant confining pressure of 30 MPa (i.e., an effective pressure of 15 MPa) but at various constant differential stresses of 138, 140, 142, 144, and 146 MPa. Figure 17 shows the numerically obtained creep curves for these five simulations, and Fig. 18 shows the numerically obtained creep strain rates against time curves. The simulated creep

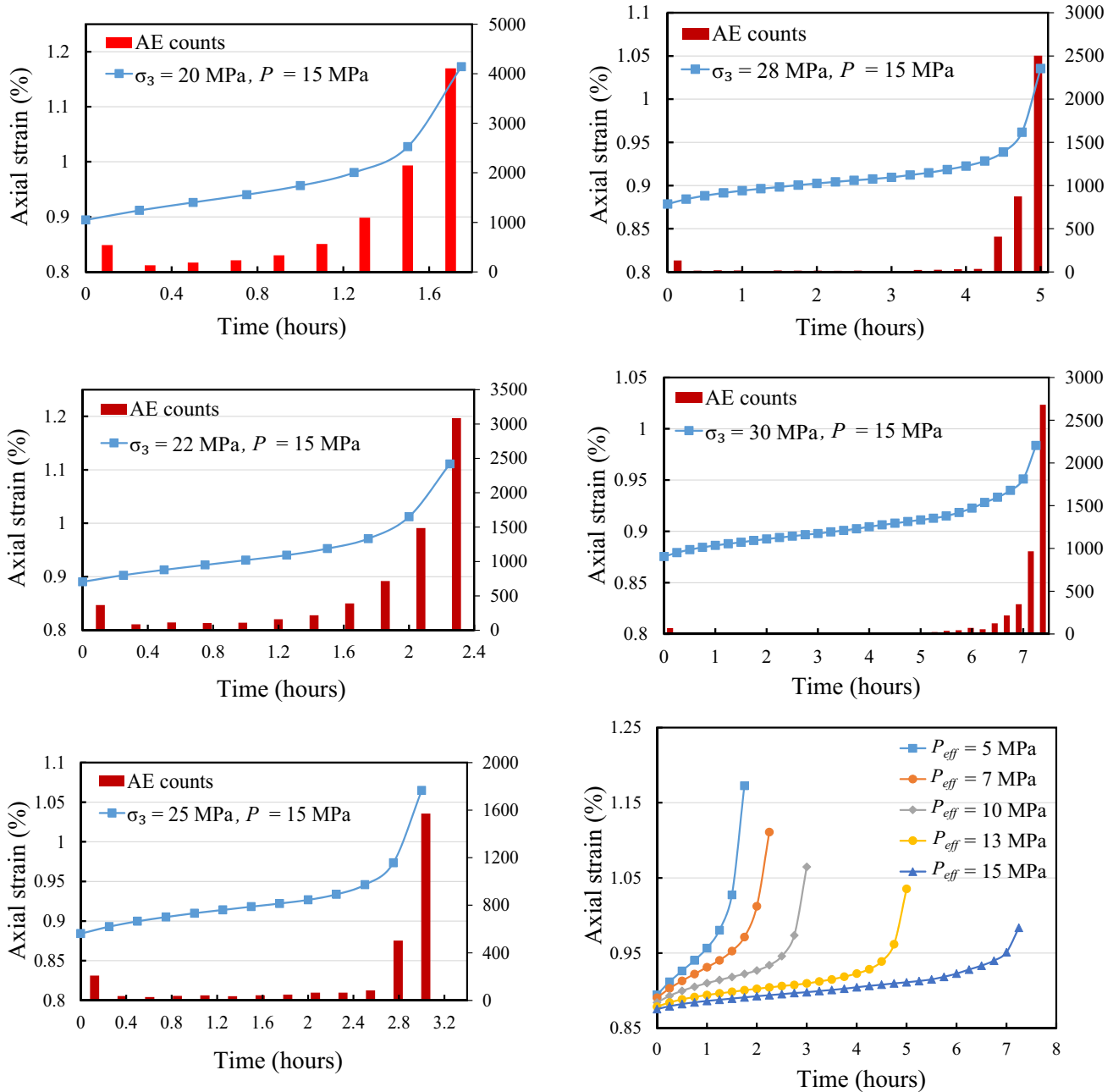


Fig. 15 Axial creep and AE activity curves for simulated rock samples at constant pore pressure of 15 MPa and various constant confining pressures of 20, 22, 25, 28, and 30 MPa (i.e., effective pressures

of 5, 7, 10, 13, and 15 MPa). The same constant applied differential stress of 142 MPa was used in all the simulations

curves exhibit the typical decelerating–accelerating phenomenology of experimental creep curves (Brantut et al. 2013). The decelerating–accelerating phenomenology of the creep process is best observed in the plot of creep strain rate as a function of time (Fig. 18). The strain rate first decelerates to a minimum value, before accelerating to failure (Fig. 18), as observed in creep experiments on porous sandstones in the laboratory (Brantut et al. 2014a). As the differential stress increases in the simulations, the minimum strain rate

becomes higher (Fig. 18), and the time-to-failure becomes shorter (Fig. 17). For example, the time-to-failure at a differential stress of 138 MPa is more than 11 h, but the time-to-failure at 146 MPa is only about 5.5 h (Fig. 17). The simulated times-to-failure in semi-log space as a function of applied differential stress curves are plotted in Fig. 19. It is clearly seen that even a modest increase in differential stress can significantly alter the magnitude of the creep strain rate (Fig. 18) and the time-to-failure (Fig. 19). The results of the

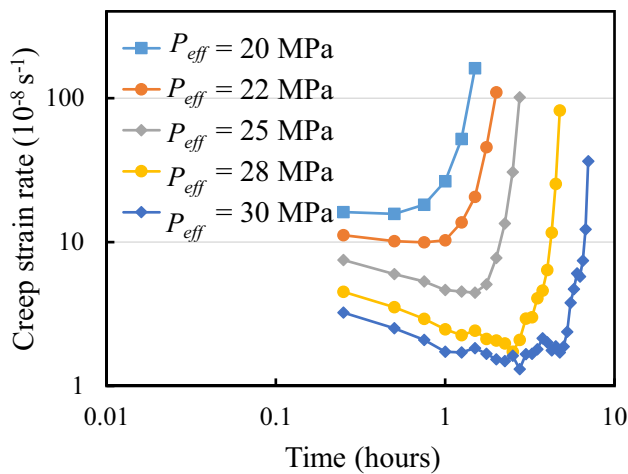


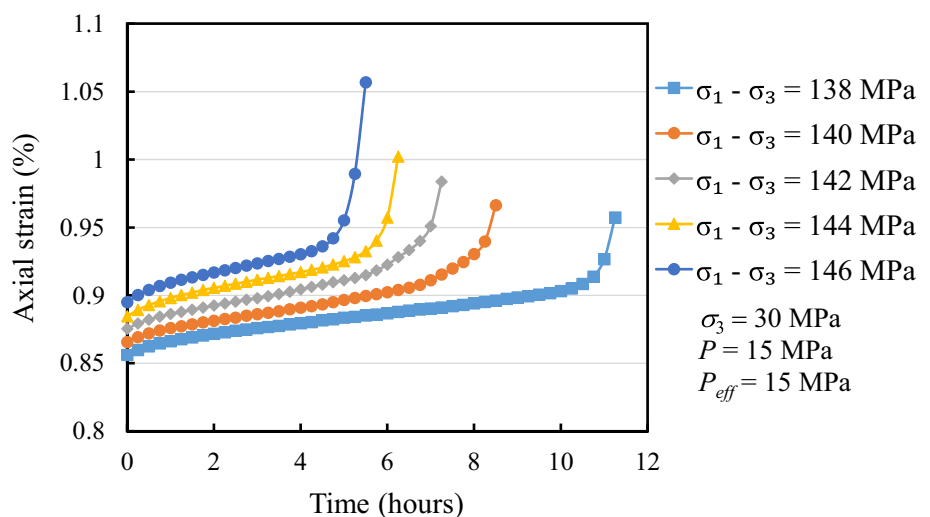
Fig. 16 Simulated creep strain rate versus time curves for numerical specimens deformed at a constant pore pressure of 15 MPa and various constant confining pressures of 20, 22, 25, 28, and 30 MPa (i.e., effective pressures of 5, 7, 10, 13, and 15 MPa). The same constant applied differential stress of 142 MPa was used in all the simulations

simulations are in line with the many experimental studies that report on the influence of differential stress on brittle creep strain rate (see Brantut et al. 2013 for a review).

5.4 Effect of Sample Homogeneity

It is well known that rock is a heterogeneous material. It is for this reason we use a Weibull statistical distribution to reproduce mechanical heterogeneity within a realistic rock medium. We recall here that we use the Weibull distribution to provide heterogeneity in the strength (compressive and tensile) and Young’s modulus of the sample at the mesoscale. To examine the effect of the value of homogeneity index on brittle creep, a set of simulations performed on rock samples with different homogeneity indices ($\chi=6, 7, \text{ and } 8$)

Fig. 17 Axial strain versus time curves (i.e., creep curves) for simulated rock samples at constant confining pressure of 30 MPa and a constant pore pressure of 15 MPa and various constant differential stresses of 138, 140, 142, 144, and 146 MPa. All simulations were performed under the same input parameters



but at the same effective pressure of 15 MPa (confining pressure = 30 MPa, pore pressure = 15 MPa) and the same constant applied differential stress of 142 MPa were performed. Figures 20, 21, and 22 show axial strain, AE activity, final failure patterns, and creep strain rate as a function of time for these three simulations. It is seen that an increase in homogeneity index leads to a decrease in creep strain rate of the specimen (Fig. 22) and a corresponding increase in time-to-failure (Figs. 20, 21, 22). For example, the minimum creep rate is $7.11 \times 10^{-8} \text{ s}^{-1}$ when the sample homogeneity index is $\chi=6$, while the minimum creep strain rate is decreased to $1.77 \times 10^{-8} \text{ s}^{-1}$ when the homogeneity index is increased to $\chi=8$. The corresponding times-to-failure are 3.25 and 7.25 h, respectively. Such observations can be explained by the fact that the peak strength of a more homogeneous rock sample is higher. These simulations could be analogous to performing brittle creep experiments on, for example, granites containing progressively more microcracks or limestones that contain progressively more microporosity.

6 Conclusions

We have presented a numerical hydro-mechanical model for brittle creep to replicate time-dependent brittle deformation of heterogeneous brittle rock (here demonstrated for red sandstone) under loading conditions at different constant pores and confining pressures. To reflect the material heterogeneity at the mesoscale, the mechanical parameters (e.g., strength and Young’s modulus) of the mesoscopic material elements, which are assumed to be homogeneous and isotropic, are assigned randomly using a Weibull statistical distribution. The model introduces the concept of a mesoscopic renormalization to capture the co-operative interaction between microcracks in the transition from distributed to localized damage. We have validated our model

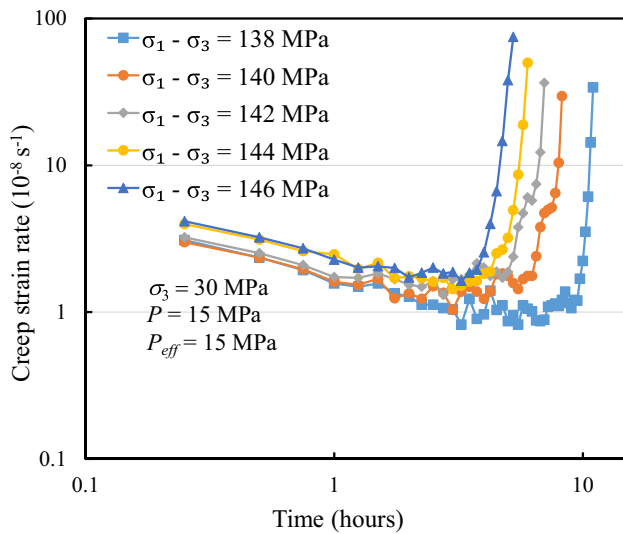


Fig. 18 Simulated strain rate versus time curves of numerical specimens at constant confining pressure of 30 MPa and a constant pore pressure of 15 MPa and various constant differential stresses of 138, 140, 142, 144, and 146 MPa. All simulations were performed under the same input parameters

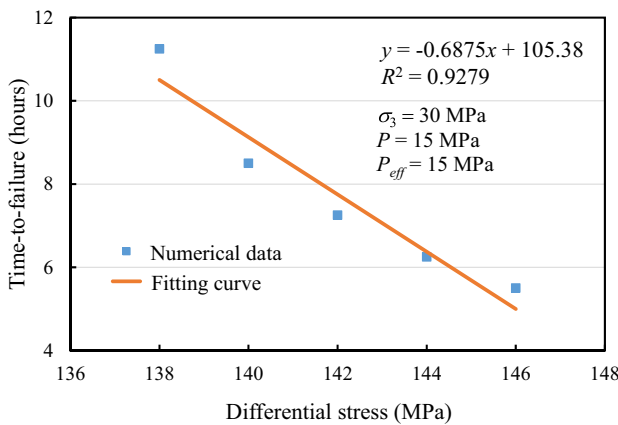


Fig. 19 Semi-log plot of time-to-failure against differential stress of numerical specimens for the simulated creep tests performed at constant confining pressure of 30 MPa and a constant pore pressure of 15 MPa and various constant differential stresses (from 138 to 146 MPa)

against time-independent and time-dependent experimental data and then used it to simulate conventional brittle creep experiments at various constant pores and confining pressures and at various applied differential axial stresses. The simulation results adequately replicate typical observations of creep tests including the acceleration to failure. In addition, the influence of sample homogeneity on creep behavior was also studied.

Our simulations show, in line with experimental observations, that (1) creep strain rate is decreased and

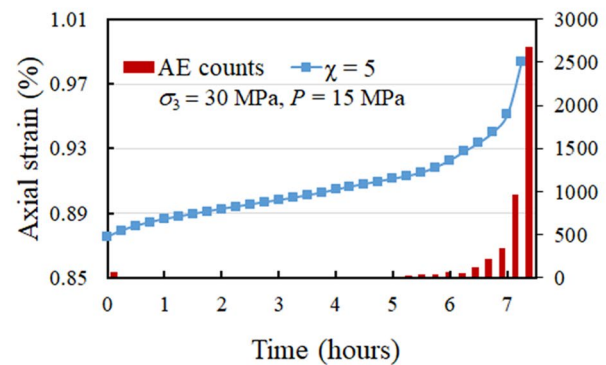
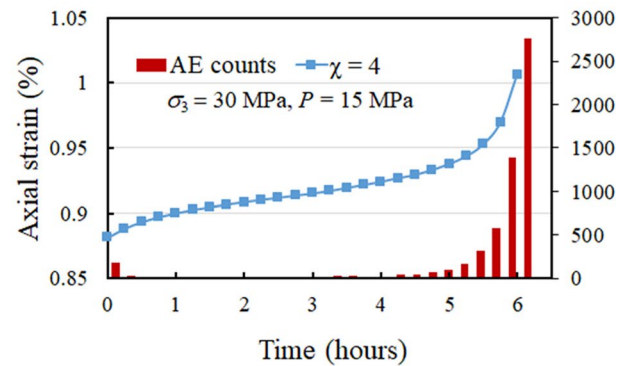
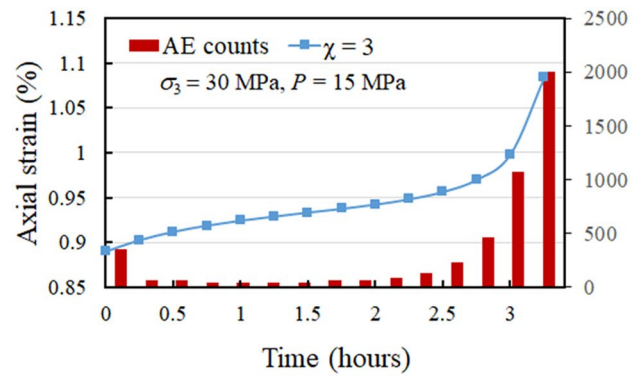


Fig. 20 Axial creep strain and AE activity curves for simulated rock samples with various homogeneity indices (from 3 to 5) at constant differential stress of 142 MPa and effective pressure of 15 MPa (confining pressure = 15 MPa, pore pressure = 15 MPa)

time-to-failure is increased when the effective pressure is increased (for a given differential stress and sample homogeneity), (2) creep strain rate is increased and time-to-failure is decreased when the differential stress is increased (for a given effective pressure and sample homogeneity), and (3) creep strain rate is decreased and time-to-failure is increased when the sample homogeneity is increased (for a given differential stress and effective pressure). We find that the proposed model reproduces the progressive development of fracture processes and the evolution of failure morphology in heterogeneous rocks during brittle creep.

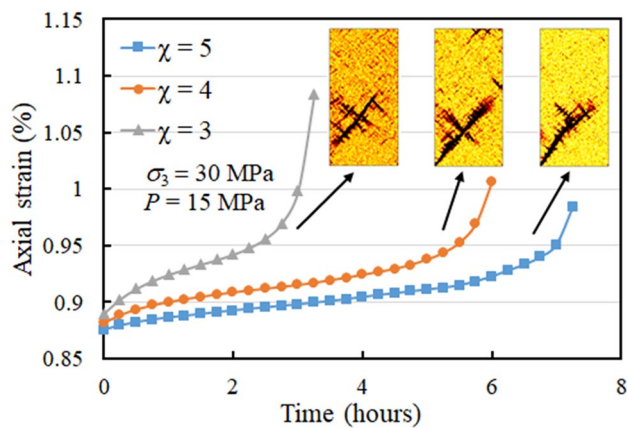


Fig. 21 Axial creep strain curves for simulated rock samples with various homogeneity indices (from 3 to 5) at constant differential stress of 142 MPa and effective pressure of 15 MPa (confining pressure = 15 MPa, pore pressure = 15 MPa). Snapshots of the sample failure are also provided; the dark colors in the numerical specimen are the damage-induced fractures. (Colour figure online)

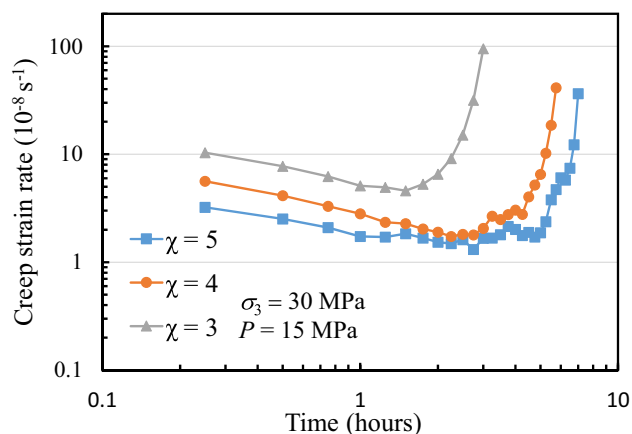


Fig. 22 Simulated creep strain rate versus time curves for numerical specimens with various homogeneity indices (from 3 to 5) at constant differential stress of 142 MPa and effective pressure of 15 MPa (confining pressure = 15 MPa, pore pressure = 15 MPa)

This model provides insight into the creep process of brittle rocks. Importantly, the simulations accurately capture the decelerating–accelerating phenomenology of a classic experimental creep curve. We therefore contend that, based on these validations, our time-dependent model is not only able to characterize the progressive time-independent damage up to failure, but also reveals the time-dependent damage evolution for sandstone under different conditions (i.e., different pore and confining pressures and different applied differential axial stresses). The presented procedure allows us to investigate the hydro-mechanical time-dependent response of inhomogeneous rock under

external loading and to glean a deeper understanding of rock failure processes at the meso- and macroscale.

Acknowledgements The support provided by Natural Science Foundation of China (Grant Nos. 51474051, 41672301 and 51761135102), National Basic Research Program (973) of China (Grant No. 2014CB047100), Fundamental Research Funds for the Central Universities of China (N150102002), and the Partenariats Hubert Curien (PHC) Cai Yuanpei Grant (Grant No. 36605ZB) are highly acknowledged. The comments of two reviewers helped improve the clarity of this manuscript.

References

- Aker E, Kühn D, Vavryčuk V, Soldal M, Oye V (2014) Experimental investigation of acoustic emissions and their moment tensors in rock during failure. *Int J Rock Mech Min Sci* 70:286–295
- Amitrano D, Helmstetter A (2006) Brittle creep, damage, and time to failure in rocks. *J Geophys Res B* 111:1–17
- Andrade E, Randall R (1949) The Rehbinder effect. *Nature* 164:1127
- Atkinson BK (1984) Subcritical crack growth in geological materials. *J Geophys Res* 89:4077–4114
- Atkinson BK, Meredith PG (1981) Stress corrosion cracking of quartz: a note on the influence of chemical environment. *Tectonophysics* 77:T1–T11
- Baud P, Meredith PG (1997) Damage accumulation during triaxial creep of Darley Dale sandstone from pore volumetry and acoustic emission. *Int J Rock Mech Min Sci* 34:24.e21–24.e10
- Baud P, Zhu W, Wong TF (2000) Failure mode and weakening effect of water on sandstone. *J Geophys Res* 105:16371–16389
- Baud P, Reuschlé T, Ji Y, Cheung CSN, Wong T-F (2015) Mechanical compaction and strain localization in Bleurswiller sandstone. *J Geophys Res* 120:6501–6522
- Bell AF, Greenhough J, Heap MJ, Main IG (2011a) Challenges for forecasting based on accelerating rates of earthquakes at volcanoes and laboratory analogues. *Geophys J Int* 185:718–723
- Bell AF, Naylor M, Heap MJ, Main IG (2011b) Forecasting volcanic eruptions and other material failure phenomena: an evaluation of the failure forecast method. *Geophys Res Lett* 38:165–176
- Biot MA (1956) General solutions of equations of elasticity and consolidation for a porous material. *J Appl Phys* 23:91–96
- Brantut N, Baud P, Heap MJ, Meredith PG (2012) Micromechanics of brittle creep in rocks. *J Geophys Res Solid Earth* 117:B8
- Brantut N, Heap MJ, Meredith PG, Baud P (2013) Time-dependent cracking and brittle creep in crustal rocks: a review. *J Struct Geol* 52:17–43
- Brantut N, Heap MJ, Baud P, Meredith PG (2014a) Mechanisms of time-dependent deformation in porous limestone. *J Geophys Res* 119:5444–5463
- Brantut N, Heap MJ, Baud P, Meredith PG (2014b) Rate- and strain-dependent brittle deformation of rocks. *J Geophys Res* 119:1818–1836
- Carter NL, Hansen FD (1983) Creep of rock salt. *Tectonophysics* 92:275–333
- Chen W, Konietzky H (2014) Simulation of heterogeneity, creep, damage and lifetime for loaded brittle rocks. *Tectonophysics* 633:164–175
- Cristescu ND (1993) A general constitutive equation for transient and stationary creep of rock salt. *Int J Rock Mech Min Sci Geomech Abstr* 30:125–140
- Dubey RK, Gairola VK (2008) Influence of structural anisotropy on creep of rock salt from Simla Himalaya, India: an experimental approach. *J Struct Geol* 30:710–718

- Duda M, Renner J (2012) The weakening effect of water on the brittle failure strength of sandstone. *Geophys J Int* 192:1091–1108
- Farquharson J, Heap MJ, Baud P, Reuschlé T, Varley NR (2016) Pore pressure embrittlement in a volcanic edifice. *Bull Volcanol* 78:1–19
- Fortin J, Stanchits S, Dresen G, Gueguen Y (2009) Acoustic emissions monitoring during inelastic deformation of porous sandstone: comparison of three modes of deformation. *Pure Appl Geophys* 166:823–841
- Golshani A, Okui Y, Oda M, Takemura T (2006) A micromechanical model for brittle failure of rock and its relation to crack growth observed in triaxial compression tests of granite. *Mech Mater* 38:287–303
- Heap MJ, Baud P, Meredith PG (2009a) Influence of temperature on brittle creep in sandstones. *Geophys Res Lett* 36:L19305
- Heap MJ, Baud P, Meredith PG, Bell AF, Main IG (2009b) Time-dependent brittle creep in Darley Dale sandstone. *J Geophys Res* 114:1–22
- Heap MJ, Baud P, Meredith PG, Vinciguerra S, Bell AF, Main IG (2011) Brittle creep in basalt and its application to time-dependent volcano deformation. *Earth Planet Sci Lett* 307:71–82
- Heap MJ, Brantut N, Baud P, Meredith PG (2015) Time-dependent compaction band formation in sandstone. *Br J Forensic Pract* 11:3–7
- Heard HC (1976) Comparison of the flow properties of rocks at crustal conditions. *Philos Trans R Soc Lond A* 283:173–186
- Homand-Etienne F, Hoxha D, Shao JF (1998) A continuum damage constitutive law for brittle rocks. *Comput Geotech* 22:135–151
- Jaeger JC, Cook NGW, Zimmerman R (eds) (2007) *Fundamentals of rock mechanics*. Wiley-Blackwell, Singapore
- Karrech A, Schrank C, Freij-Ayoub R, Regenauer-Lieb K (2014) A multi-scaling approach to predict hydraulic damage of poromaterials. *Int J Mech Sci* 78:1–7
- Katz O, Reches Z (2002) Pre-failure damage, time-dependent creep and strength variations of a brittle granite. In: *Proceedings of the fifth international conference on anal discontinuous deformation*. Ben-Gurion University, Balkema, Rotterdam
- Kranz RL (1980) The effects of confining pressure and stress difference on static fatigue of granite. *J Geophys Res* 85:1854–1866
- Kranz RL, Scholz CH (1977) Critical dilatant volume of rocks at the onset of tertiary creep. *J Geophys Res* 82:4893–4898
- Kranz RL, Harris WJ, Carter NL (1982) Static fatigue of granite at 200 °C. *Geophys Res Lett* 9:1–4
- Kraus H (1980) *Creep analysis*. Wiley, New York
- Lajtai E, Schmidtker R, Bielus L (1987) The effect of water on the time-dependent deformation and fracture of a granite. *Int J Rock Mech Min Sci Geomech Abstr.* 24:24–255
- Lemaitre J, Desmorat R (2005) *Engineering damage mechanics*. Springer, Berlin
- Li X, Konietzky H (2014) Numerical simulation schemes for time-dependent crack growth in hard brittle rock. *Acta Geotech* 10:1–19
- Li X, Konietzky H, Li X (2016) Numerical study on time dependent and time independent fracturing processes for brittle rocks. *Eng Fract Mech* 163:89–107
- Lin QX, Liu YM, Tham LG, Tang CA, Lee PKK, Wang J (2009) Time-dependent strength degradation of granite. *Int J Rock Mech Min Sci* 46:1103–1114
- Lockner D (1993a) The role of acoustic-emission in the study of rock fracture. *Int J Rock Mech Min Sci* 30:883–899
- Lockner D (1993b) Room temperature creep in saturated granite. *J Geophys Res* 98:475–487
- Lockner DA, Madden TR (1991) A multiple-crack model of brittle-fracture. 2. Time-dependent simulations. *J Geophys Res* 96:19643–19654
- Lu Y, Elsworth D, Wang L (2014) A dual-scale approach to model time-dependent deformation, creep and fracturing of brittle rocks. *Comput Geotech* 60:61–76
- Mallet C, Fortin J, Guéguen Y, Bouyer F (2015) Brittle creep and sub-critical crack propagation in glass submitted to triaxial conditions. *J Geophys Res Solid Earth* 120(2):879–893
- Maranini E, Brignoli M (1999) Creep behavior of a weak rock: experimental characterization. *Int J Rock Mech Min Sci* 36(1):127–138
- Maranini E, Yamaguchi T (2001) A non-associated viscoplastic model for the behavior of granite in triaxial compression. *Mech Mater* 33:283–293
- Meredith PG, Atkinson BK (1983) Stress corrosion and acoustic emission during tensile crack propagation in Whin Sill dolerite and other basic rocks. *Geophys J Int* 75:1–21
- Nicolas A, Fortin J, Regnet JB, Verberne BA, Plümper O, Dimanov A, Spiers CJ, Guéguen Y (2017) Brittle and semi-brittle creep of Tavel limestone deformed at room temperature. *J Geophys Res* 122:4436–4459
- Ngwenya B, Main I, Elphick S, Crawford B, Smart B (2001) A constitutive law for low-temperature creep of water-saturated sandstones. *J Geophys Res* 106:21811–21826
- Ohnaka M (1983) Acoustic emission during creep of brittle rock. *Int J Rock Mech Min Sci Geomech Abstr* 20:121–134
- Okubo S, Fukui K, Hashiba K (2010) Long-term creep of water-saturated tuff under uniaxial compression. *Int J Rock Mech Min Sci* 47:839–844
- Pan Z, Wan-xie Z (1991) The parametric variational principle for Perzyna model in viscoplasticity. *Appl Math Mech* 12:433–437
- Pellet F, Hajdu A, Deleruyelle F, Besnus F (2005) A viscoplastic model including anisotropic damage for the time dependent behavior of rock. *Int J Numer Anal Methods Geomech* 29:941–970
- Peng T-R, Wang C-H, Hsu S-M, Wang G-S, Su T-W, Lee J-F (2010) Identification of groundwater sources of a local-scale creep slope: using environmental stable isotopes as tracers. *J Hydrol* 381:151–157
- Perzyna P (1966) Fundamental problems in viscoplasticity. *Adv Appl Mech* 9:243–377
- Perzyna P (1971) Thermodynamic theory of viscoplasticity. *Adv Appl Mech* 11:313–354
- Schubnel A, Walker E, Thompson BD, Fortin J, Guéguen Y, Young RP (2006) Transient creep, aseismic damage and slow failure in Carrara marble deformed across the brittle-ductile transition. *Geophys Res Lett* 33:L17301
- Shao JF, Deveau G, Hoteit N, Sibai M, Bart M (1997) Time dependent continuous damage model for deformation and failure of brittle rock. *Int J Rock Mech Min Sci* 34:285.e281–285.e213
- Shao JF, Zhu QZ, Su K (2003) Modeling of creep in rock materials in terms of material degradation. *Comput Geotech* 30:549–555
- Shao JF, Chau KT, Feng XT (2006) Modeling of anisotropic damage and creep deformation in brittle rocks. *Int J Rock Mech Min Sci* 43:582–592
- She C, Xuan C (2010) Influence of high pore water pressure on creep properties of rock. *Chin J Rock Mech Eng* 29:1603–1609
- Sterpi D, Giorda G (2009) Visco-plastic behavior around advancing tunnels in squeezing rock. *Rock Mech Rock Eng* 42:319–339
- Tang CA (1997) Numerical simulation of progressive rock failure and associated seismicity. *Int J Rock Mech Min Sci* 34:249–261
- Vasseur J, Wadsworth FB, Lavallée Y, Bell AF, Main IG, Dingwell DB (2015) Heterogeneity: the key to failure forecasting. *Sci Rep* 5:13259
- Vasseur J, Wadsworth FB, Heap MJ, Main IG, Lavallée Y, Dingwell DB (2017) Does an inter-flaw length control the accuracy of rupture forecasting in geological materials? *Earth Planet Sci Lett* 475:181–189

- Voight B (1989) A relation to describe rate-dependent material failure. *Science* 243:200–203
- Wang WM, Sluys LJ, De Borst R (2015) Viscoplasticity for instabilities due to strain softening and strain-rate softening. *Int J Numer Meth Eng* 40:3839–3864
- Wasantha PLP, Ranjith PG, Shao SS (2014) Energy monitoring and analysis during deformation of bedded-sandstone: use of acoustic emission. *Ultrasonics* 54:217–226
- Weibull W (1951) A statistical distribution function of wide applicability. *J Appl Mech* 18:293–297
- Weiss J, Marsan D (2003) Three-dimensional mapping of dislocation avalanches: clustering and space/time coupling. *Science* 299:89–92
- Weng MC, Tsai LS, Liao CY, Jeng FS (2010) Numerical modeling of tunnel excavation in weak sandstone using a time-dependent anisotropic degradation model. *Tunn Undergr Space Technol* 25:397–406
- Wong T-F, David C, Zhu W (1997) The transition from brittle faulting to cataclastic flow in porous sandstones: mechanical deformation. *J Geophys Res* 102:3009–3025
- Wong TF, Wong RHC, Chau KT, Tang CA (2006) Microcrack statistics, Weibull distribution and micromechanical modeling of compressive failure in rock. *Mech Mater* 38:664–681
- Xu P, Yang S-Q (2016) Permeability evolution of sandstone under short-term and long-term triaxial compression. *Int J Rock Mech Min Sci* 85:152–164
- Xu T, Tang C, Zhao J, Li L, Heap MJ (2012) Modelling the time-dependent rheological behavior of heterogeneous brittle rocks. *Geophys J Int* 189:1781–1796
- Xu T, Zhou GL, Heap MJ, Zhu WC, Chen CF, Baud P (2017) The influence of temperature on time-dependent deformation and failure in granite: a mesoscale modeling approach. *Rock Mech Rock Eng* 50:2345–2364
- Yang S-Q, Jing H-W, Cheng L (2014) Influences of pore pressure on short-term and creep mechanical behavior of red sandstone. *Eng Geol* 179:10–23
- Yoshida H, Horii H (1992) A micromechanics-based model for creep behavior of rock. *Appl Mech Rev* 45:294–303
- Zhu YY, Cescotto S (1995) A fully coupled elasto-visco-plastic damage theory for anisotropic materials. *Int J Solids Struct* 32:1607–1641
- Zhu WC, Wei J, Zhao J, Niu LL (2014) 2D numerical simulation on excavation damaged zone induced by dynamic stress redistribution. *Tunn Undergr Space Technol* 43:315–326

Publisher's Note Springer Nature remains neutral with regard to jurisdictional claims in published maps and institutional affiliations.